

Excitonic Resonance Effects and Davydov Splitting in Circularly Polarized Raman Spectra of Few-Layer WSe₂

Sanghun Kim¹, Kangwon Kim¹, Jae-Ung Lee, and Hyeonsik Cheong

Department of Physics, Sogang University, Seoul 04107, Korea

E-mail: hcheong@sogang.ac.kr

Keywords: Raman spectroscopy, Circularly polarized Raman measurement, Resonance Raman measurement, Tungsten diselenide, WSe₂.

Notes: ¹These authors contributed equally.

Abstract

Few-layer tungsten diselenide (WSe₂) is investigated using circularly polarized Raman spectroscopy with up to eight excitation energies. The main E_{2g}¹ and A_{1g} modes near 250 cm⁻¹ appear as a single peak in the Raman spectrum taken without consideration of polarization but are resolved by using circularly polarized Raman scattering. The resonance behaviors of the E_{2g}¹ and A_{1g} modes are examined. Firstly, both the E_{2g}¹ and A_{1g} modes are enhanced near resonances with the exciton states. The A_{1g} mode exhibits Davydov splitting for trilayers or thicker near some of the exciton resonances. The low-frequency Raman spectra show shear and breathing modes involving rigid vibrations of the layers and also exhibit strong dependence on the excitation energy. An unidentified peak at ~19 cm⁻¹ that does not depend on the number of layers appears near resonance with the B exciton state at 1.96 eV (632.8 nm). The strengths of the intra- and inter-layer interactions are estimated by comparing the mode frequencies and Davydov splitting with the linear chain model, and the contribution of the next-nearest-neighbor interaction to the inter-layer interaction turns out to be about 34% of the nearest-neighbor interaction. Fano resonance is observed for 1.58-eV excitation, and its origin is found to be the interplay between two-phonon scattering and indirect band transition.

1. Introduction

Transition metal dichalcogenides (TMDs) are drawing much attention for possible application as optoelectronic devices, especially for flexible devices [1–3]. Raman spectroscopy is extensively used as a fast and non-destructive characterization tool to study the structural properties of TMDs [4,5]. On the other hand, the optical properties of TMDs are heavily modulated by the excitonic effect because of large exciton binding energies on the order of a few hundred meV [6–10]. The excitonic effects influence Raman scattering through various resonance-related effects, resulting in a number of intriguing phenomena [11–20]. Therefore, it is crucial to be able to distinguish Raman features specific to resonance conditions from those that are intrinsic vibrational features. Although TMDs share many similarities such

as indirect-to-direct gap transition from bulk to monolayer, strongly coupled valley-spin, and a large exciton binding energy [6–10, 21–24], there exists subtle differences depending on the combination of transition metal and chalcogen elements. For example, the lowest-energy exciton states in WS₂ and WSe₂ are dark excitons whereas the corresponding states in MoS₂ and MoSe₂ are bright [8,25]. Similarly, resonance Raman behaviors of the TMDs have many common features such as strong resonance and activation of forbidden modes at some exciton states, which depends on the compound. For example, the strong resonance behavior is observed at the A exciton state of MoS₂ [12] but in MoSe₂, the strongest resonance is observed at the C exciton state [17,18]. Furthermore, Davydov splitting of the intralayer vibration mode due to interlayer interaction has been reported for MoSe₂, MoTe₂, and WS₂ only [15,17,19,26–30]. Since WSe₂ has a relatively small exciton transition energy (~1.65 eV for monolayer) compared with other TMDs, it is often used to form heterostructures with other TMDs [31–33]. Therefore, it is important to establish the basic physical properties of this material. Furthermore, comparing different resonance behaviors of similar TMD materials might shed light on the origin of novel phenomena observed in these materials.

Monolayer WSe₂ comprises a tungsten layer sandwiched between selenium layers, covalently bonded to one another to form a trilayer (TL), in a hexagonal 1H structure [34]. Each TL is bonded by relatively weak van der Waals interaction with neighboring TLs and is stacked in such a way that the selenium atoms on the second layer sit right on top of the tungsten atoms on the first layer to form a so-called 2H structure [35], which is the most stable polytype [34,36]. Figure 1(a) shows the crystal structure of 2H-WSe₂. Due to the weak interaction between the TLs, it can be easily cleaved. Monolayer (1TL) WSe₂ is a direct band gap semiconductor with the lowest energy optical transition at 1.65 eV near the *K* or *K'* point of the Brillouin zone. For 2TL or thicker, the band structure is indirect, but the direct-gap photoluminescence is still visible [37,38]. The optical absorption spectrum of WSe₂ is dominated by four peaks: at ~1.65, ~2.1, ~2.4, and ~2.9 eV for 1TL. Some research groups identified them as A, B, A', and B' excitons, where the A exciton is formed between the conduction band minima and the top of the valence band at the *K* or *K'* points and the B exciton between the conduction band minima and the spin-

orbit split valence band. A' and B' are described as the excited states of A and B excitons, respectively [11,37,39–41]. However, other groups assigned them to four independent excitonic states of A, B, C, and D excitons [42–44], where the C exciton is formed between states in the $K\Gamma$ direction of the Brillouin zone, and the D exciton originates from the same bands as the B exciton along the KM direction. The origins of these excitonic states are neither well established yet nor the focus of this work. Nevertheless, we will use the notation of A, B, C, and D excitons since there does not seem to be an obvious correlation between A and B excitons and A' and B' excitons. The A, C, and D peaks in the absorption spectrum redshift with increasing number of layers, whereas the B peak does not shift appreciably [37]. The resonance effects, when the excitation laser energy is close to these excitonic peak energies, are systematically studied in this work.

Davydov splitting in TMDs is lifting of the degeneracy in the *intralayer* vibrational modes due to *interlayer* interactions and has been observed in MoTe₂, MoSe₂, and WS₂ [15,17–19,26–30]. Since the splitting directly correlates with the interlayer coupling, it is a good indicator of interlayer interaction in layered materials. Furthermore, Davydov splitting affects the Raman selection rule of the mode so as to make some forbidden modes become allowed in few-layer cases. It has been found that the relative intensities of the split peaks change drastically depending on the layer number and the excitation laser energy, usually near excitonic resonances [15,17,29]. Therefore, it is convenient to combine the study of the resonance effects with that of Davydov splitting. In this work, we studied the Raman spectra of 1 to 8 TL WSe₂ using 8 different excitation energies to study the resonance effects and Davydov splitting. In order to resolve the main intralayer modes with similar frequencies, we employ circularly polarized Raman scattering. From the measured Raman mode frequencies and Davydov splitting, the force constants of interlayer and intralayer interactions are estimated.

2. Method

Few-layer WSe₂ samples were prepared by mechanically exfoliating on Si substrates with a 285-nm SiO₂ layer from single-crystal bulk WSe₂ flakes (HQ Graphene) (see supplementary information

for representative optical microscope images). The number of TLs was confirmed by combination of optical contrast, Raman, and PL measurements (see supplementary information for the PL spectra of few-layer WSe₂ [26,37,38,45]). Micro-Raman measurements were performed with eight different excitation sources: the 325 and 441.6 nm (3.82 and 2.81 eV) lines of a He-Cd laser; the 457.9, 488, and 514.5 nm (2.71, 2.54, and 2.41 eV, respectively) lines of an Ar⁺ laser; the 532 nm (2.33 eV) line of a diode-pumped-solid-state (DPSS) laser; the 632.8 nm (1.96 eV) line of a He-Ne laser; and the 784.8 nm (1.58 eV) line of a diode laser. The laser beam was focused onto a sample by a 50× microscope objective lens (0.8 N.A.) for all excitation wavelengths except for the 325 nm excitation for which a 40× UV objective lens (0.5 N.A.) was used. The scattered light was collected and collimated by the same objective and dispersed by a Jobin-Yvon Horiba iHR550 spectrometer (1200 grooves/mm for 784.8 nm and 2400 grooves/mm for all the other excitation wavelengths). For detecting the signal, a liquid-nitrogen-cooled back-illuminated charge-coupled-device (CCD) detector was used. To access the low-frequency range below 50 cm⁻¹, volume holographic filters (Ondax and OptiGrate) were used to clean the laser lines and reject the Rayleigh-scattered light. The laser power was kept below 50 μW in order to avoid local heating of the sample. The spectral resolution ranged between 0.3 cm⁻¹ (1.96 eV) and 1.5 cm⁻¹ (3.82 eV). In order to extract the intrinsic resonance effects, the Raman intensities were calibrated by the intensity of the Si Raman peak at 520 cm⁻¹ for each excitation energy to correct for the efficiency of the detection system. In addition, the interference effects due to multiple reflection from the substrate [46] and the resonance Raman effects of Si [47] are considered. The wavelength dependent refractive indices are taken from the measured values for 1TL WSe₂ [42]. Because of the limitations of available data, bulk values [48] were used for the refractive indices in the UV region (for the excitation wavelength of 325 nm). The detailed calibration procedure has been published elsewhere [12]. Figure 1(b) shows the schematic of the circularly polarized Raman measurement system. For the circularly polarized light, we use a polarizer and a quarter wave plate before the objective lens. The scattered light from the sample passes through the same quarter-wave plate, becoming linearly polarized in parallel or orthogonal direction depending on the

circular polarization. The analyzer selects the polarization component, and a half-wave plate is used to keep the polarization of the light entering the spectrometer the same regardless of the analyzer direction.

3. Results and Discussion

Figure 1(c) is an (unpolarized) Raman spectrum of 4TL WSe₂ measured with the excitation energy of 2.54 eV (488 nm). The peaks marked by ‘*’ are due to Brillouin scattering from the Si substrate. In the low-frequency region (<50 cm⁻¹), there are shear (blue circles) and breathing (red triangles) modes, which correspond to the in-plane and out-of-plane direction interlayer vibrations, respectively [45,49]. In the high frequency region (100–400 cm⁻¹), four first order Raman modes are observed: E_{1g} (~175 cm⁻¹), E_{2g}¹ (~248 cm⁻¹), A_{1g} (~251 cm⁻¹), and A_{2u} (~308 cm⁻¹) modes. Since the point symmetry groups of bulk and few-layer WSe₂ are *D*_{6h} for bulk, *D*_{3h} for all odd TLs, and *D*_{3d} for all even TLs, the mode notations should be different depending on the number of TLs even though they originate from similar vibrational modes [28,35,45,49]. For simplicity, however, we will use the bulk notations in the following discussion regardless of the number of TLs. The E_{1g} mode is Raman active but forbidden in backscattering for bulk and odd-TL WSe₂. However, a small signal from this mode is observed regardless of the number of TLs except for the monolayer case (see supplementary information figures S2-S4) because a significant portion of the incident and scattered light is not normal to the sample plane due to the large numerical aperture. The A_{2u} mode is infrared active and Raman inactive, but for few-layer WSe₂, there is a small Davydov splitting of this mode due to interlayer interaction. Some of the split modes are Raman active, and therefore there is a finite Raman signal in the vicinity of the A_{2u} mode. Since the splitting is very small, the Davydov split peak appears at the same frequency as the main A_{2u} peak. Other weak peaks are also observed. The weak signals at ~220 cm⁻¹ and ~268 cm⁻¹ have been assigned to the E-mode at the *K*-point, E(*K*), and the A mode at the *M*-point, A(*M*), respectively [11,38]. In addition, the signal near ~260 cm⁻¹ is ascribed to 2-phonon scattering of the longitudinal acoustic phonon at the *M* point [2LA(*M*)], the

peaks at 360 cm^{-1} and 373 cm^{-1} to the sum of LO and TO phonon of E_{2g}^1 mode and LA at the M -point [$E_{2g}^1, LO(M)+LA(M)$ and $E_{2g}^1, TO(M)+LA(M)$], respectively, and the signal at $\sim 393\text{ cm}^{-1}$ to $3LA(M)$ [11,38,50].

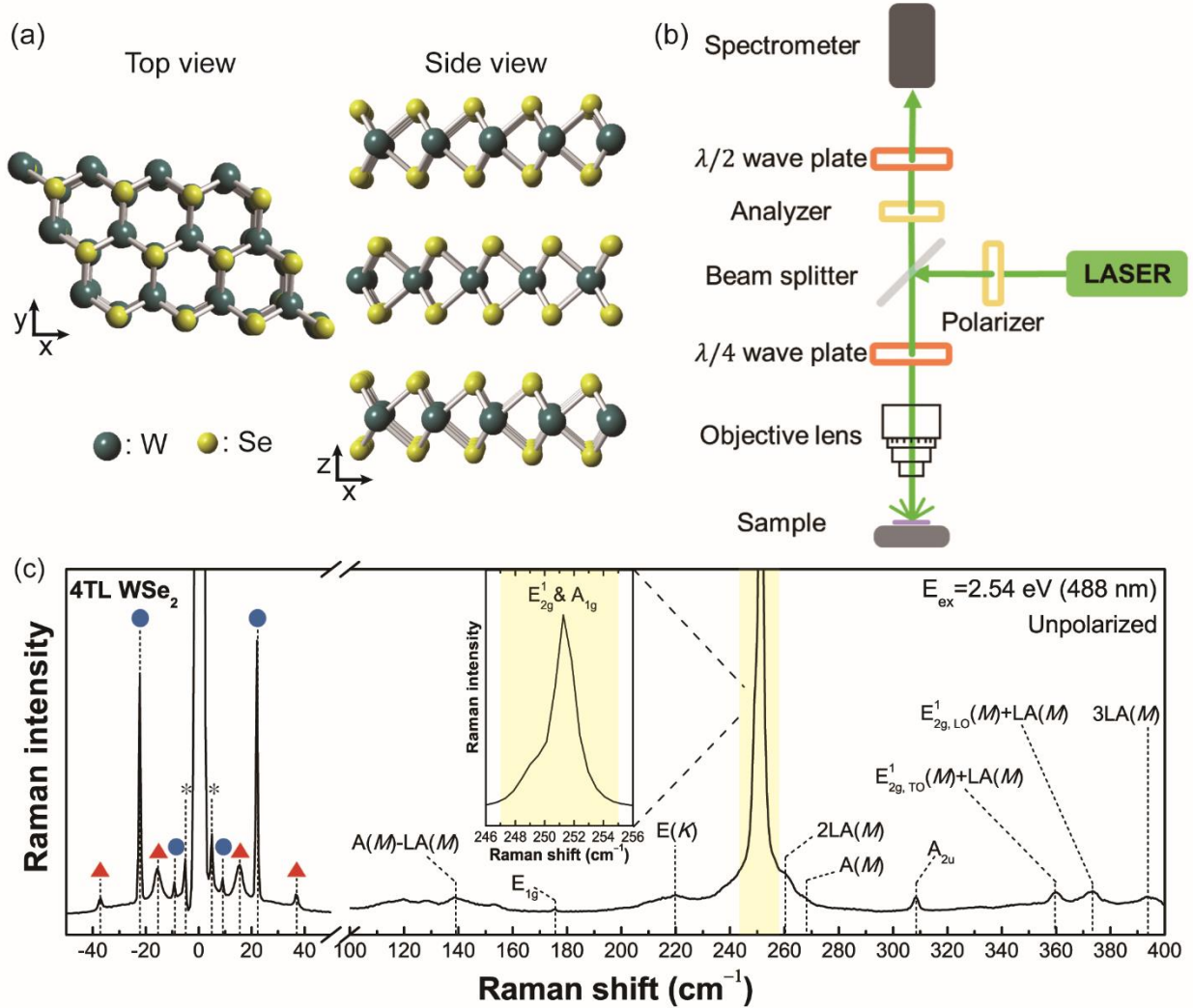


Figure 1. (a) Crystal structure of 2H-WSe₂. (b) Schematic of the circularly polarized Raman measurement system. (c) Unpolarized Raman spectrum of 4TL WSe₂ measured with excitation energy of 2.54 eV (488 nm).

The E_{2g}^1 and A_{1g} modes have similar frequencies and so are not resolved. In order to resolve these two peaks, circularly polarized Raman scattering is utilized [51]. If σ_i and σ_o represent the

circular polarizations of the incident and outgoing photons, respectively, the Raman cross section is proportional to $\left| \langle \sigma_o | R | \sigma_i \rangle \right|^2$, where R represents the Raman tensor of the mode. Circularly polarized light

propagating in the z direction is represented by $\sigma_{\pm} = \frac{1}{\sqrt{2}} \begin{pmatrix} 1 \\ \mp i \\ 0 \end{pmatrix}$. The Raman tensor of the A_{1g} mode is

given by $R = \begin{pmatrix} a & 0 & 0 \\ 0 & a & 0 \\ 0 & 0 & b \end{pmatrix}$ for all TLs. For the case of the same circular polarization in backscattering

geometry [$(\sigma + \sigma +)$ or $(\sigma - \sigma -)$], the intensity of the A_{1g} mode is proportional to $\left| \langle \sigma_o | R | \sigma_i \rangle \right|^2 = a^2$.

On the other hand, if σ_o and σ_i are opposite [$(\sigma + \sigma -)$ or $(\sigma - \sigma +)$],

$\left| \langle \sigma_o | R | \sigma_i \rangle \right|^2 = \left| \langle \sigma + | R | \sigma - \rangle \right|^2 = 0$. Therefore, the A_{1g} mode is observed only in the same circular

polarization configurations. Meanwhile, the Raman tensors of the E_{2g}^1 modes are given by

$R = \begin{pmatrix} 0 & -d & 0 \\ -d & 0 & 0 \\ 0 & 0 & 0 \end{pmatrix}$ or $R = \begin{pmatrix} d & 0 & 0 \\ 0 & -d & 0 \\ 0 & 0 & 0 \end{pmatrix}$ for bulk or odd TLs and $R = \begin{pmatrix} 0 & -c & -d \\ -c & 0 & 0 \\ -d & 0 & 0 \end{pmatrix}$ or

$R = \begin{pmatrix} c & 0 & 0 \\ 0 & -c & d \\ 0 & d & 0 \end{pmatrix}$ for even TLs. In either case, $\left| \langle \sigma + | R | \sigma + \rangle \right|^2 = \left| \langle \sigma - | R | \sigma - \rangle \right|^2 = 0$, whereas

$\left| \langle \sigma + | R | \sigma - \rangle \right|^2 = \left| \langle \sigma - | R | \sigma + \rangle \right|^2 = d^2$ or c^2 . Therefore, the E_{2g}^1 modes are observed only in the opposite

circular polarization configurations. By combining these results, we conclude that only the A_{1g} mode is

observed in the same polarization configuration and the E_{2g}^1 mode in the opposite polarization

configurations. By using circularly polarized Raman scattering, we were able to resolve the A_{1g} and E_{2g}^1

peaks and study their resonance profiles separately. We should note that in Raman scattering with linearly

polarized light, only the E_{2g}^1 mode is observed in cross polarization and both the A_{1g} and the E_{2g}^1 modes

are observed in parallel polarization. Zhao *et al.* used this method to identify the two modes for only one excitation energy (1.96 eV) [50]. However, since some of the Davydov-split peaks overlap with the E_{2g}^1 mode, Davydov splitting cannot be studied in detail if one used linear polarization.

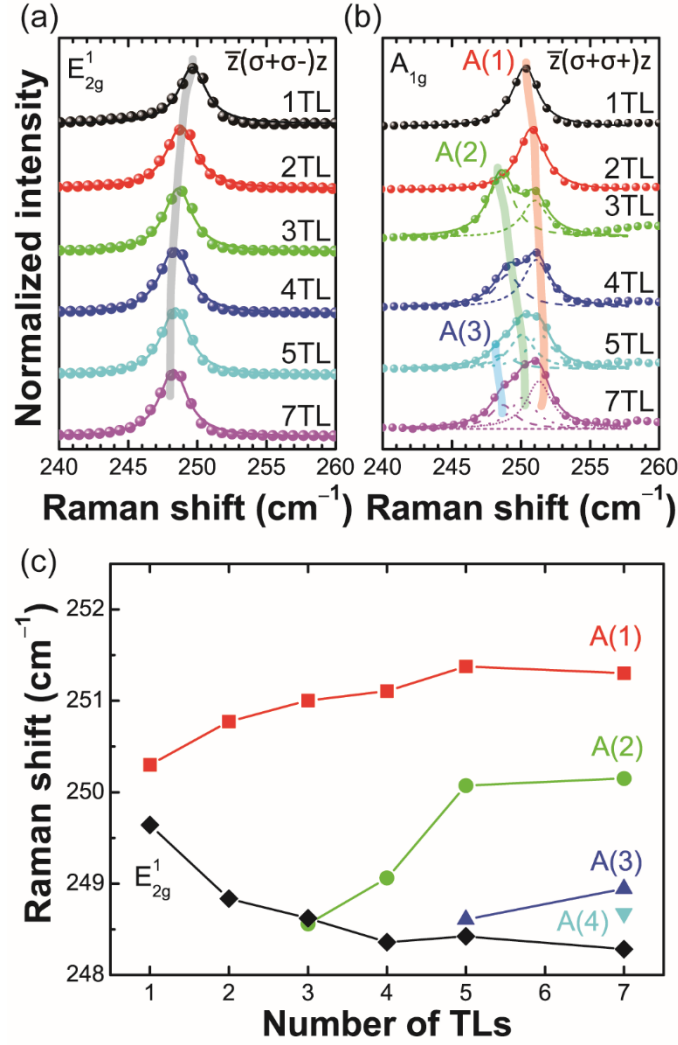


Figure 2. Circularly polarized Raman spectra of (a) the E_{2g}^1 mode and (b) A_{1g} mode measured with excitation energy of 2.81 eV (441.6 nm). Davydov-split peaks of the A_{1g} mode are resolved. (c) Peak positions as a function of the number of TLs.

Figures 2(a) and (b) show the E_{2g}^1 and A_{1g} modes separately, measured with circularly polarized light. The spectra are normalized in order to show the peak shift clearly. The E_{2g}^1 and A_{1g} modes, which correspond to in-plane vibration of transition metal and chalcogen atoms and out-of-plane symmetric

vibration of chalcogen atoms, respectively, show opposite shifts with the number of TLs: the E_{2g}^1 mode redshifts whereas the A_{1g} mode blueshifts as the number of TLs increases. The separation between these two modes can be used to identify the number of TLs as in the case of other TMDs [17,28,50,52].

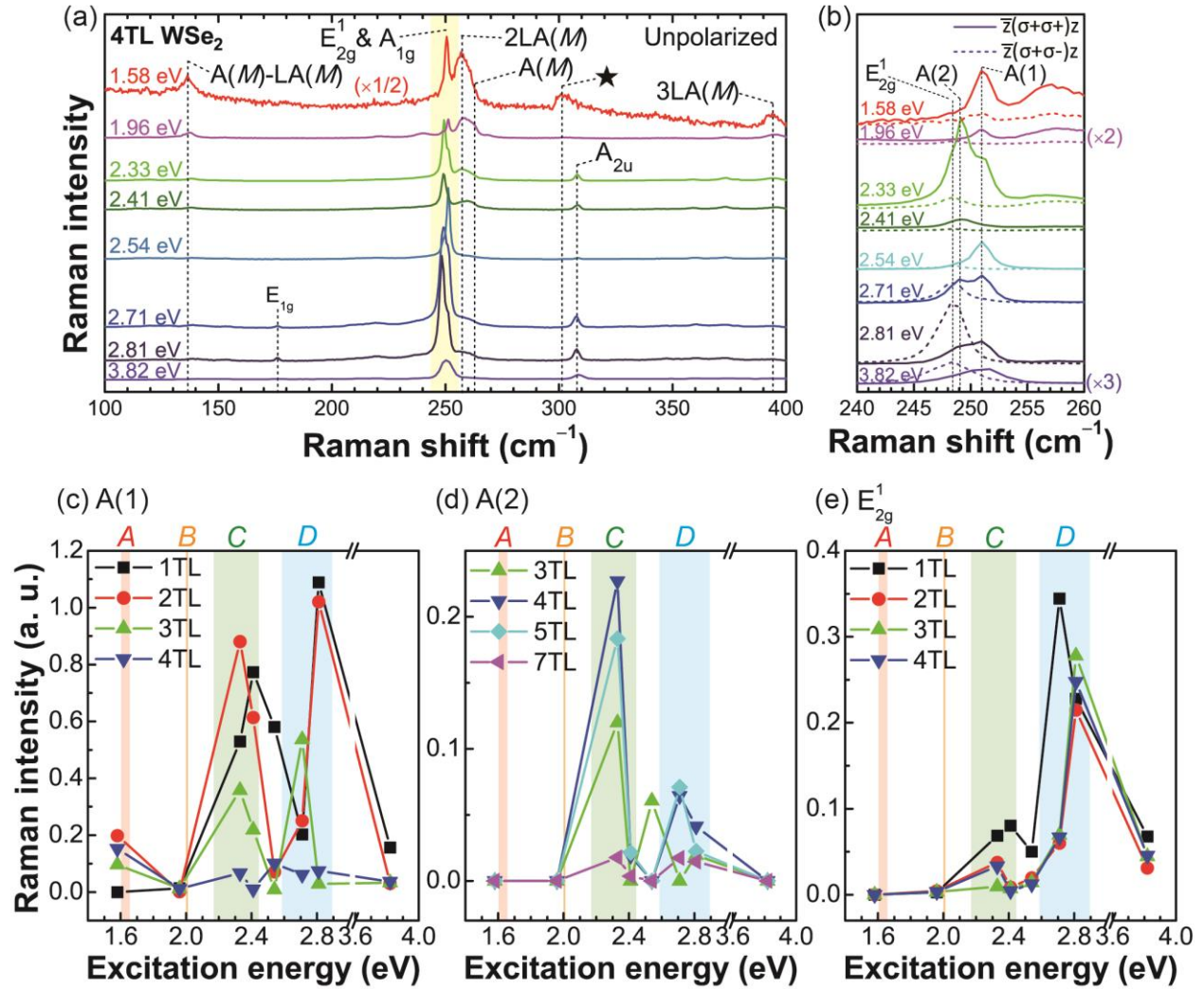


Figure 3. Raman spectra of the 4TL WSe₂ using eight excitation energies with (a) polarization-unresolved and (b) circularly polarized light. Raman intensity as a function of excitation energies for (c) the A(1), (d) A(2), and (e) E_{2g}^1 mode.

Figure 3(a) shows the Raman spectra of 4TL WSe₂ measured with 8 different excitation energies without polarization optical components (see supplementary information figures S2-S4 for other

TLs and figures S5-S7 for TL dependence of the spectrum for each excitation energy). The line shape of the unresolved peak of main E_{2g}^1 and A_{1g} modes varies greatly depending on the excitation energy, reaffirming the importance of resolving the peaks using circular polarization. The circularly polarized Raman spectra in figure 3(b) show the resonance patterns more clearly, and we find that for some excitation energies the A_{1g} mode is divided into several peaks due to Davydov splitting [53,54]. Similar splitting has been observed in MoTe_2 , MoSe_2 , and WS_2 [15,17,18,26–30]. In general, an intralayer vibration mode of n -TL TMD splits into $n/2$ $[(n+1)/2]$ Raman active modes and $n/2$ $[(n-1)/2]$ infrared modes for even [odd] n . Figure 2(b) shows the deconvolution of the A_{1g} peak to obtain the split peaks. For example, there are two Raman active modes originating from the A_{1g} mode of 4TL, which we call A(1) and A(2) modes, in the order of higher frequency. We also observe in figure 3(b) that the relative ratio of the intensities of A(1) and A(2) depends strongly on the excitation energy. For some excitation energies, A(2) is even stronger than A(1). In general, the highest-frequency mode A(1) is always visible, but the lower frequency modes are observed only near resonance excitations [15,17,28]. Figures 3(c-e) show the resonance profiles of the A(1), A(2), and E_{2g}^1 peaks, respectively. All three peaks exhibit strong enhancement near the C and D excitons. The A(1) peaks also shows a small enhancement at the A exciton resonance. On the other hand, none of these peaks show enhancement near the B exciton resonance at ~ 2.1 eV. These results are consistent with previous resonance Raman measurements without considering polarization [11,16]. Since WSe_2 has a relatively smaller bandgap among TMDs, resonance behaviors near the C and D excitons can be more easily examined using available laser lines. Upon close inspection, we find subtle yet important differences between A and E_{2g}^1 modes. For example, the D resonance of the A(1) peak seems to shift to lower energy as the number of TLs increases. On the other hand, that for the E_{2g}^1 peak shifts to slightly higher energy as the number of TL increases. This difference cannot be noticed without resolving the two peaks by using circular polarization. Since the D exciton energy is known to decrease with thickness [37], the resonance profile of the A(1) peak is consistent with being due to resonance with the D exciton state. However, the thickness dependence of the resonance profile of the E_{2g}^1 peak suggests that this resonance may have a different origin. For example, this resonance can be due

to transitions between the lower valence band and the higher conduction band at Γ (midpoint between K and L) or transitions at the K point between the valence band minima and the higher conduction bands. Furthermore, we also observe that the Davydov-split A(2) peak is strongly enhanced for resonance with the C exciton state, which might shed light on the origin of the enhancement of lower-frequency Davydov-split peaks at specific excitation energies. Although Davydov splitting is common to many TMDs, the resonance conditions for it seems to depend on the material. For WS₂, Davydov splitting is enhanced near the A exciton resonance at ~ 2.0 eV [27]. On the other hand, the splitting was observed for all excitation energies greater than 1.8 eV for MoTe₂ [15,28,29]. In the case of MoSe₂ and WSe₂, Davydov splitting is clearly observed near resonance with the C excitons or the band-to-band transition [17,18]. Since the A_{1g} mode in which Davydov splitting is observed involves vibrations of only the chalcogen atoms, the resonance enhancement of Davydov splitting depends on the kind of chalcogen atoms rather than the transition metal. Further studies are needed to develop a consistent theory that can explain these differences.

As noted before, the (forbidden) E_{1g} mode at ~ 175 cm⁻¹ is clearly observed at higher excitation energies except for the monolayer case. We should mention that this peak is not visible in the case of 3.82 eV excitation because we used a smaller NA objective for this excitation energy. The A_{2u} mode at ~ 308 cm⁻¹ is observed for excitation energies greater than 2 eV, but its intensity is conspicuously smaller for the 2.54 eV excitation. We note that at this excitation energy, the Davydov-split peaks of the main A_{1g} mode are also very weak. This confirms our earlier interpretation the A_{2u} mode is visible due to Davydov splitting [17]. Both the 2LA(M) and A(M) signals seem to be enhanced for lower excitation energies (see supplementary information figure S8 for complete resonance profiles for 1–4 TL). At 1.96 eV, for example, the combination of these peaks has a higher intensity than the main E_{2g}¹ and A_{1g} modes. This enhancement correlates with resonance with the A and B exciton states near 1.65 and 2.1 eV, respectively. Del Corro *et al.* also reported enhancement of these peaks at the B exciton resonance [11,16]. Similar dramatic

enhancement of the multi-phonon scattering signal near resonance has been observed for MoS₂ near A and B exciton resonances [12,55].

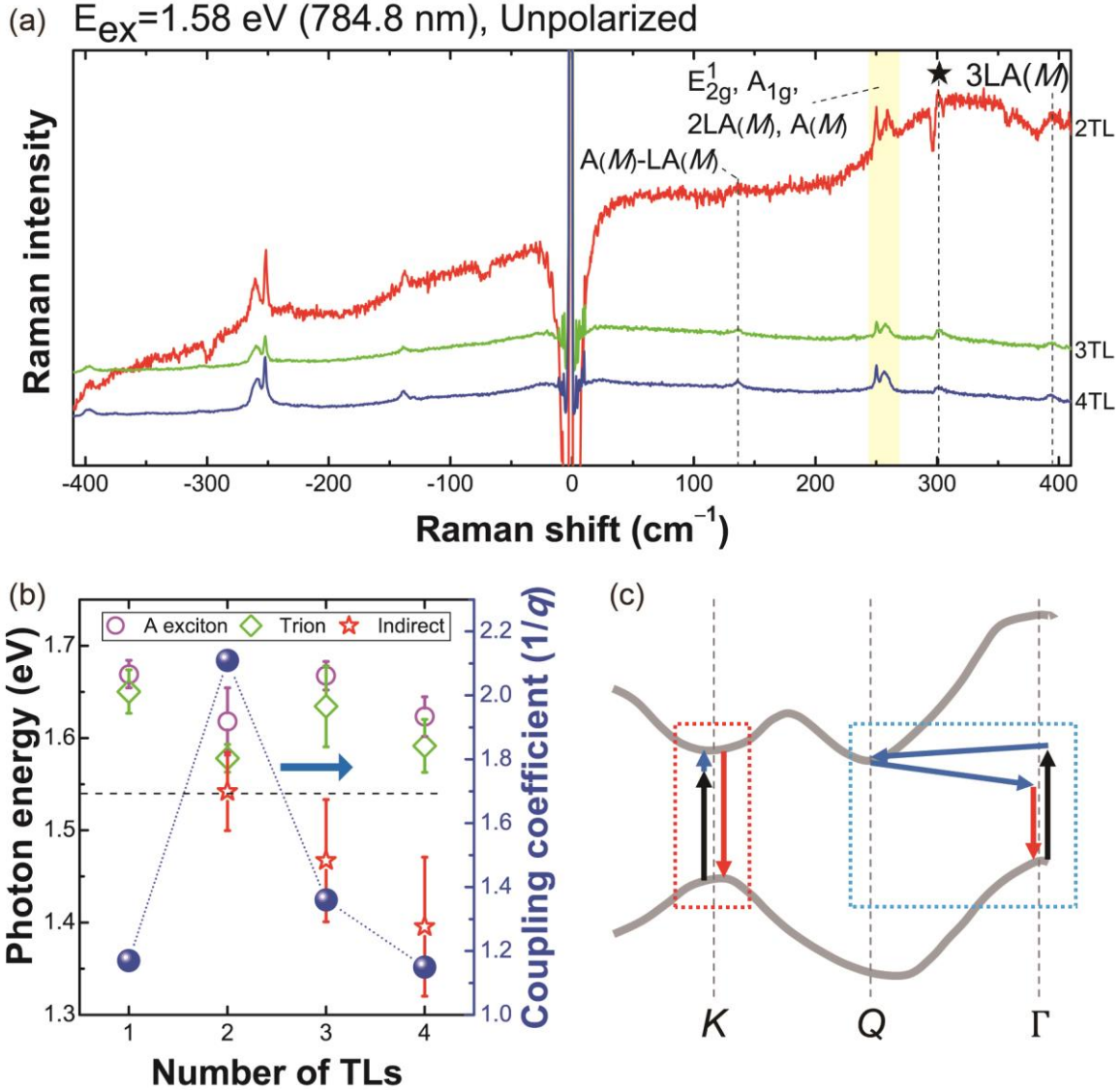


Figure 4. (a) Anti-Stokes and Stokes Raman spectra of 2–4 TL WSe₂ measured with 1.58 eV excitation energy. (b) Photon energies of A exciton, charged exciton (trion), and indirect gap and coupling coefficient ($1/q$) as a function of the number of TLs. Black dashed line at 1.54 eV shows the scattered photon energy of the BWF line. (c) Schematics of outgoing resonance Raman process at K -point (red dotted box) and resonance Raman process from Γ - to Q -point (blue dotted box) responsible for Fano resonance.

For 1.58 eV excitation, we found that the anti-Stokes Raman peaks are stronger than the Stokes Raman peaks for 2TL or thicker (see figure 4(a) and supplementary figure S9), which implies that the anti-Stokes signal is in outgoing resonance. Since the phonon energies of A_{1g} or the E_{2g}^1 mode are ~ 30 meV, the outgoing resonance condition is met if the resonant state has an energy of ~ 1.61 eV, which in fact is close to the A exciton state for 2TL or thicker. We also observe a Breit-Wigner-Fano (BWF) type [56] signal at ~ 301 cm^{-1} only for the 1.58 eV excitation regardless of the number of TLs, indicating a Fano-like resonance (see supplementary information for other TLs). This resonance is most prominent for 2TL (see supplementary figure S10). Fano resonance is a quantum interference of a discrete excitation with a continuum and has been observed in TMDs only for a low-frequency shear mode of WS_2 [19,20]. The BWF line shape is represented by [57],

$$I(\omega) = I_0 \frac{[1 + 2(\omega - \omega_0)/(q\Gamma)]^2}{[1 + 4(\omega - \omega_0)^2/\Gamma^2]}, \quad (1)$$

where Γ is the broadening parameter, $1/q$ is the coupling constant, and ω_0 is the peak frequency of uncoupled mode. The coupling coefficients $1/q$ obtained from fitting the spectra (see supplementary figure S10) are 1.17, 2.11, 1.36, and 1.15 for 1–4 TL WSe_2 , respectively, as shown in figure 4(b). Unlike the other phonon modes, the Stokes signal of this BWF line is stronger than the anti-Stokes signal, which indicates that the origin of this Fano resonance is different from the resonance Raman scattering process of the other Raman peaks. In order to analyze Fano resonance, one needs to identify the discrete and continuum excitations responsible for it. For the discrete excitation, phonon emission is a natural candidate. Since there is no phonon mode at this frequency, it should be a combination of two or more phonons. In order to identify the continuum excitation, we examined the PL spectra of 1–4 TL WSe_2 . The PL signal contains contributions from the exciton, a charged exciton (trion) and the indirect transition (see supplementary figure S11), and figure 4(b) summarizes their energies. For 2TL WSe_2 , the indirect gap energy (1.54 eV) coincides with the energy of the Raman scattered photon from the BWF line [dashed line in figure 4(b)].

Since Fano resonance is most pronounced for 2TL, this coincidence is an important clue. According to theoretical calculations [58], the indirect transition occurs between the valence band maximum at the Γ point and the conduction band minimum at the Q point between Γ and K points of the Brillouin zone as shown in figure 4(c). We also find that the position of this peak (301 cm^{-1}) is close to the sum of the $E_{\text{lg,LO}}$ and ZA phonons at the Q -point [$E_{\text{lg,LO}}(Q)+ZA(Q)$] [38]. Based on these observations, we can infer that the Fano resonance is due to the resonance Raman process from Γ -point of the valence band to Q -point the conduction band as shown in blue dotted box in figure 4(c). Since this process is independent of the A exciton state formed at the K point [red dotted box in figure 4(c)], this Fano resonance does not have the same resonance behavior as the other Raman modes that exhibit outgoing resonances. This interpretation is supported by the fact that the coupling coefficient $1/q$ correlates with the proximity of the indirect gap transition energy to the scattered photon energy as demonstrated in figure 4(b).

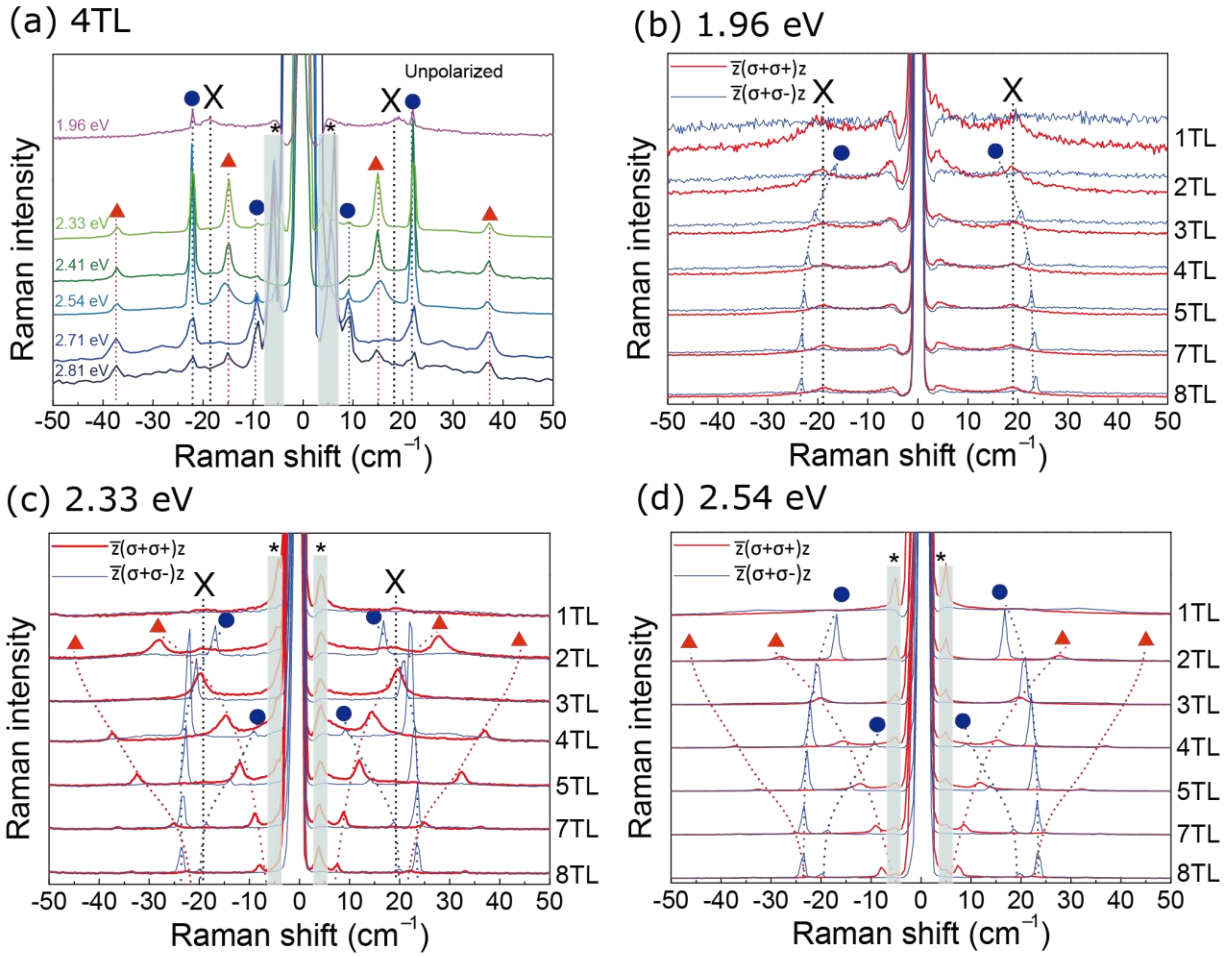


Figure 5. (a) Low-frequency Raman spectra of 4TL WSe₂ measured with six different laser energies. Shear (●) and breathing (▲) modes are indicated. Dependence of low-frequency circularly-polarized Raman spectrum on number of TLs for excitation energies of (b) 1.96 eV, (c) 2.33 eV, and (d) 2.54 eV. For 1.96 eV and 2.33 eV excitations, an unidentified peak (X) appears for all thicknesses.

Figure 5(a) shows the unpolarized low-frequency Raman spectra of 4TL WSe₂ measured with six different excitation energies. The shear and breathing modes are clearly seen, but the relative intensities depend on the excitation energy (see supplementary information figure S8 for resonance profiles of these modes). Figures 4(b-d) show the dependence of the low frequency spectrum on the number of TLs for three excitation energies, respectively. Here, 1.96 eV is close to the B exciton resonance and 2.33 eV to the C exciton resonance, whereas 2.54 eV corresponds to the off-resonance case. Circularly polarized Raman scattering is employed to resolve the breathing ($\sigma+\sigma+$) and the shear

($\sigma+\sigma-$) modes. The strong dependence of the peak positions on the number of TLs can be used as a definitive measure of the number of Ts. In addition, we observe a clear signal at 19 cm^{-1} for the 1.96 eV excitation for all TLs. This peak also appears weakly for the 2.33 eV excitation, and its position does not depend on the number of TLs. Similar low-frequency peaks have been observed in MoS_2 and WS_2 [12,19,20], but there are important differences. Although two such peaks are observed in WS_2 [19,20], there is no indication of a second peak in WSe_2 . Also, unlike the case of MoS_2 where this peak is observed for both same ($\sigma-\sigma-$) and opposite ($\sigma-\sigma+$) circular polarization configurations [12], this peak in WSe_2 is observed only for the same circular polarization configuration. Also, the small spin-orbit splitting of the conduction band was suggested as the origin of this peak in MoS_2 [59], but the corresponding splitting in WS_2 or WSe_2 are much larger. For WS_2 , there has been a suggestion that the two such peaks are from acoustic phonons (TA and LA) with a specific momentum value [19]. This interpretation was based partly on the ratio of two mode frequencies which is close to the ratio of LA/TA mode frequencies, but it was not obvious what determines the specific value of momentum regardless of the number of TLs. At the moment, there is no consistent model that can explain the origin of these peaks, and so we tentatively label it as an ‘X’ peak. Since it appears only near excitonic resonances, a new kind of collective excitation of the excitons could be the origin, but more studies are needed.

From the positions of the shear and breathing modes, one can calculate the in-plane and out-of-plane interlayer force constants using the linear chain model [45,49]. We obtained the in-plane force constant of $3.06 \times 10^{19}\text{ Nm}^{-3}$ and the out-of-plane force constant of $8.56 \times 10^{19}\text{ Nm}^{-3}$ by considering only the nearest-neighbor interaction between adjacent Se layers. These values are similar to those from previous work [45]. In the case of out-of-plane vibrations, the calculations can be refined by including the Davydov-split peak positions and including the next-nearest-neighbor interactions [17,28] and the surface effect [60]. The detailed calculation procedure is described in Refs. [17] and [28]. By fitting the peak positions of the out-of-plane Raman modes, breathing, A_{1g} including Davydov splitting, and A_{2u} including Davydov splitting (see supplementary information figure S12), we obtained the out-of-plane force

constants of WSe₂. The fitting results are shown in figure 5, and the obtained parameters are summarized in table 1. The force constant for the nearest-neighbor interlayer interaction (β) between Se atoms of the adjacent layer is $4.80 \times 10^{19} \text{ Nm}^{-3}$, which is only half the value obtained in the simple linear chain model that included only the nearest-neighbor interaction. The force constant for the next-nearest-neighbor interlayer interaction (γ) between the Se atoms and the W atoms in the adjacent layer is $1.65 \times 10^{19} \text{ Nm}^{-3}$, which amounts to about 34 % of the nearest-neighbor interlayer interaction (β). This is somewhat larger than those in MoTe₂ (~ 20 %) [28] and MoSe₂ (~ 30%) [17].

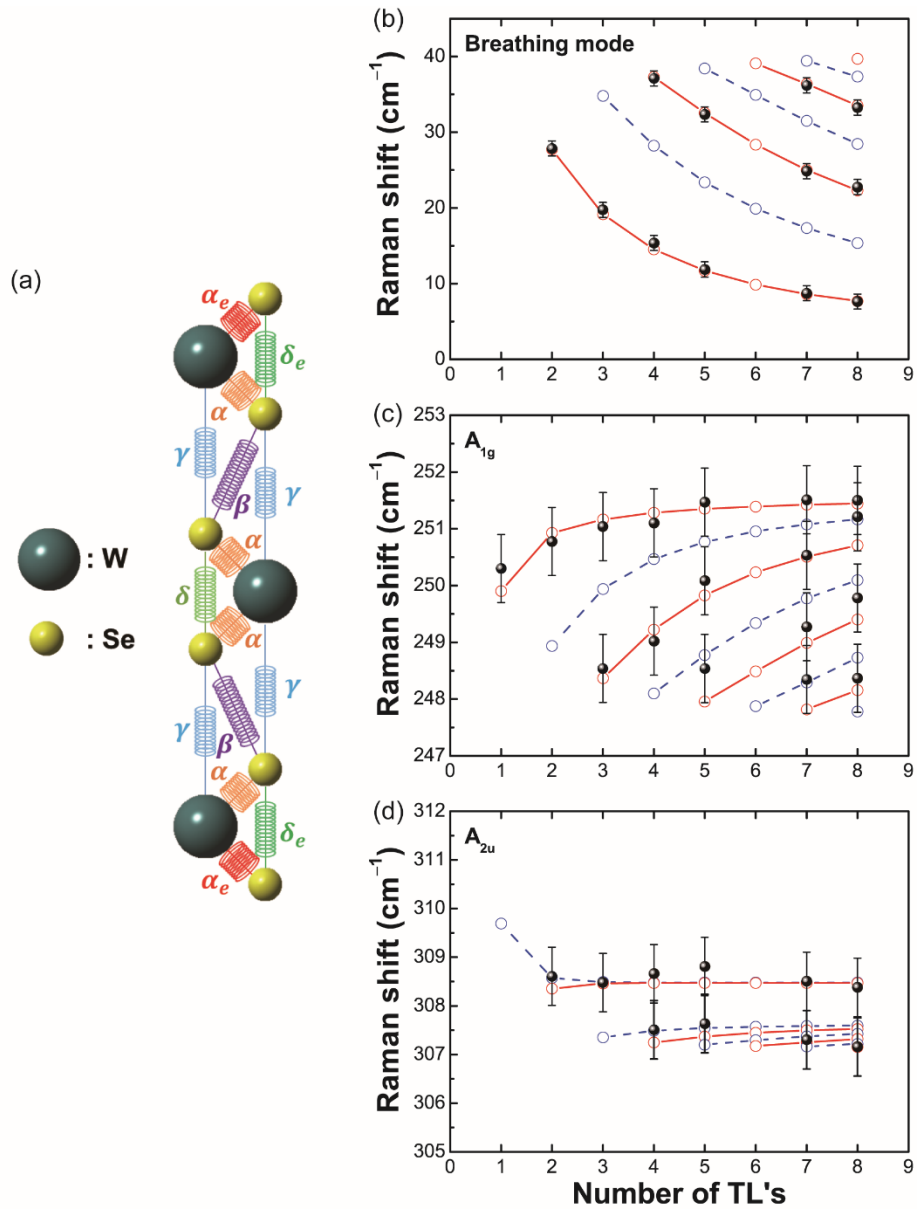


Figure 6. (a) Force constants in linear chain model. Out-of-plane Raman modes as a function of the number of TLs: (b) breathing, (c) A_{1g}, and (d) A_{2u} modes. Experimental data are represented by filled circles, and open circles indicate calculated values. Red and blue data represent Raman active and inactive modes, respectively.

Table 1. Out-of-plane direction force constants per unit area of WSe₂ obtained by fitting experimental data to simple linear chain model (LCM) and a model including next-nearest-neighbor interactions.

	Corresponding interaction	Simple LCM	Including next-nearest-neighbor interaction
α (10^{19} N/m ³)	Intra-layer W-Se	312.5±0.3	249.0±0.3
α_e (10^{19} N/m ³)	Intra-layer W-Se for surface Se	310.1±0.3	255.3±0.3
β (10^{19} N/m ³)	Inter-layer Se-Se	8.56	4.80±0.2
γ (10^{19} N/m ³)	Inter-layer W-Se		1.65±0.05
δ (10^{19} N/m ³)	Intra-layer Se-Se		26.0±0.4
δ_e (10^{19} N/m ³)	Intra-layer Se-Se for surface Se		26.9±0.4

4. Conclusion

The intralayer E_{2g}¹ and A_{1g} modes of few-layer WSe₂ near 250 cm⁻¹ are resolved by using circularly polarized Raman scattering, and their resonance behaviors are examined for eight excitation energies. Both the modes are enhanced near resonances with the exciton states, and the A_{1g} mode exhibits Davydov splitting for trilayers or thicker near some of the exciton resonances. The low-frequency Raman spectra also show dependence of the shear and breathing mode intensities on the excitation energy. An unidentified peak at ~19 cm⁻¹ that does not depend on the number of TMs appears near resonance with the

B exciton state at 1.96 eV. The intra- and inter-layer force constants in the out-of-plane direction are estimated by comparing the mode frequencies and Davydov splitting with the linear chain model including the next-nearest-neighbor interaction. The contribution of the next-nearest-neighbor interaction amounts to about 34% of the nearest-neighbor interaction. Fano resonance which depends on the number of TLs is observed, and its origin is found to be the interplay between two-phonon scattering and indirect transition between the Γ point of the valence band and the Q point of the conduction band.

Acknowledgements

This work was supported by the National Research Foundation (NRF) grant funded by the Korean government (MSIP) (NRF-2016R1A2B3008363 and No. 2017R1A5A1014862, SRC program: vdWMRC center) and by a grant (No. 2011-0031630) from the Center for Advanced Soft Electronics under the Global Frontier Research Program of MSIP.

References

- [1] Xia F, Wang H, Xiao D, Dubey M and Ramasubramanian A 2014 Two-dimensional material nanophotonics *Nat. Photonics* **8** 899–907
- [2] Withers F, Del Pozo-Zamudio O, Mishchenko A, Rooney A P, Gholinia A, Watanabe K, Taniguchi T, Haigh S J, Geim A K, Tartakovskii A I and Novoselov K S 2015 Light-emitting diodes by band-structure engineering in van der Waals heterostructures *Nat. Mater.* **14** 301–6
- [3] Mak K F and Shan J 2016 Photonics and optoelectronics of 2D semiconductor transition metal dichalcogenides *Nat. Photonics* **10** 216–26
- [4] Zhang X, Tan Q-H, Wu J-B, Shi W and Tan P-H 2016 Review on the Raman spectroscopy of different types of layered materials *Nanoscale* **8** 6435

- [5] Saito R, Tatsumi Y, Huang S, Ling X and Dresselhaus M S 2016 Raman spectroscopy of transition metal dichalcogenides *J. Phys. Condens. Matter* **28** 353002
- [6] Qiu D Y, da Jornada F H and Louie S G 2013 Optical Spectrum of MoS₂: Many-Body Effects and Diversity of Exciton States *Phys. Rev. Lett.* **111** 216805
- [7] Chernikov A, Berkelbach T C, Hill H M, Rigosi A, Li Y, Aslan O B, Reichman D R, Hybertsen M S and Heinz T F 2014 Exciton Binding Energy and Nonhydrogenic Rydberg Series in Monolayer WS₂ *Phys. Rev. Lett.* **113** 76802
- [8] Ye Z, Cao T, O'Brien K, Zhu H, Yin X, Wang Y, Louie S G and Zhang X 2014 Probing excitonic dark states in single-layer tungsten disulphide *Nature* **513** 214–8
- [9] Klots A R, Newaz A K M, Wang B, Prasai D, Krzyzanowska H, Lin J, Caudel D, Ghimire N J, Yan J, Ivanov B L, Velizhanin K A, Burger A, Mandrus D G, Tolk N H, Pantelides S T and Bolotin K I 2014 Probing excitonic states in suspended two-dimensional semiconductors by photocurrent spectroscopy *Sci. Rep.* **4** 6608
- [10] Ugeda M M, Bradley A J, Shi S-F, da Jornada F H, Zhang Y, Qiu D Y, Ruan W, Mo S-K, Hussain Z, Shen Z-X, Wang F, Louie S G and Crommie M F 2014 Giant bandgap renormalization and excitonic effects in a monolayer transition metal dichalcogenide semiconductor *Nat. Mater.* **13** 1091–5
- [11] Corro E, Terrones H, Elias A, Fantini C, Feng S, Nguyen M A, Mallouk T E, Terrones M, Pimenta M A, Fisica D De, Federal U, Gerais D M, Carlos A A, Postal C, Horizonte B, Corro D E L and Al E T 2014 Excited Excitonic States in 1L, 2L, 3L, and Bulk WSe₂ Observed by Resonant Raman Spectroscopy *ACS Nano* **8** 9629–35

- [12] Lee J-U, Park J, Son Y-W and Cheong H 2015 Anomalous excitonic resonance Raman effects in few-layered MoS₂ *Nanoscale* **7** 3229–36
- [13] Nam D, Lee J-U and Cheong H 2015 Excitation energy dependent Raman spectrum of MoSe₂ *Sci. Rep.* **5** 17113
- [14] Carvalho B R, Malard L M, Alves J M, Fantini C and Pimenta M A 2015 Symmetry-Dependent Exciton-Phonon Coupling in 2D and Bulk MoS₂ Observed by Resonance Raman Scattering *Phys. Rev. Lett.* **114** 136403
- [15] Song Q J, Tan Q H, Zhang X, Wu J B, Sheng B W, Wan Y, Wang X Q, Dai L and Tan P H 2016 Physical origin of Davydov splitting and resonant Raman spectroscopy of Davydov components in multilayer MoTe₂ *Phys. Rev. B* **93** 115409
- [16] del Corro E, Botello-Méndez A, Gillet Y, Elias A L, Terrones H, Feng S, Fantini C, Rhodes D, Pradhan N, Balicas L, Gonze X, Charlier J-C, Terrones M and Pimenta M A 2016 Atypical Exciton–Phonon Interactions in WS₂ and WSe₂ Monolayers Revealed by Resonance Raman Spectroscopy *Nano Lett.* **16** 2363–8
- [17] Kim K, Lee J-U, Nam D and Cheong H 2016 Davydov Splitting and Excitonic Resonance Effects in Raman Spectra of Few-Layer MoSe₂ *ACS Nano* **10** 8113–20
- [18] Soubelet P, Bruchhausen A E, Fainstein A, Nogajewski K and Faugeras C 2016 Resonance effects in the Raman scattering of monolayer and few-layer MoSe₂ *Phys. Rev. B* **93** 155407
- [19] Tan Q-H, Sun Y-J, Liu X-L, Zhao Y, Xiong Q, Tan P-H and Zhang J 2017 Observation of forbidden phonons and dark excitons by resonance Raman scattering in few-layer WS₂ *Arxiv* 1704.01315

- [20] Yang J, Lee J-U and Cheong H 2017 Excitation energy dependence of Raman spectra of few-layer WS₂ *FaltChem (Accepted)*
- [21] Splendiani A, Sun L, Zhang Y, Li T, Kim J, Chim C Y, Galli G and Wang F 2010 Emerging photoluminescence in monolayer MoS₂ *Nano Lett.* **10** 1271–5
- [22] Xiao D, Liu G-B, Feng W, Xu X and Yao W 2012 Coupled Spin and Valley Physics in Monolayers of MoS₂ and Other Group-VI Dichalcogenides *Phys. Rev. Lett.* **108** 196802
- [23] Mak K F, He K, Shan J and Heinz T F 2012 Control of valley polarization in monolayer MoS₂ by optical helicity *Nat. Nanotechnol.* **7** 494–8
- [24] Zeng H, Dai J, Yao W, Xiao D and Cui X 2012 Valley polarization in MoS₂ monolayers by optical pumping *Nat. Nanotechnol.* **7** 490–3
- [25] Zhang X-X, You Y, Zhao S Y F and Heinz T F 2015 Experimental Evidence for Dark Excitons in Monolayer WSe₂ *Phys. Rev. Lett.* **115** 257403
- [26] Tonndorf P, Schmidt R, Böttger P, Zhang X, Börner J, Liebig A, Albrecht M, Kloc C, Gordan O, Zahn D R T, Michaelis de Vasconcellos S and Bratschitsch R 2013 Photoluminescence emission and Raman response of monolayer MoS₂, MoSe₂, and WSe₂ *Opt. Express* **21** 4908
- [27] Staiger M, Gillen R, Scheuschner N, Ochedowski O, Kampmann F, Schleberger M, Thomsen C and Maultzsch J 2015 Splitting of monolayer out-of-plane A₁' Raman mode in few-layer WS₂ *Phys. Rev. B* **91** 195419
- [28] Froehlicher G, Lorchat E, Fernique F, Joshi C, Molina-Sánchez A, Wirtz L and Berciaud S 2015 Unified Description of the Optical Phonon Modes in N -Layer MoTe₂ *Nano Lett.* **15** 6481–9

- [29] Grzeszczyk M, Gołasa K, Zinkiewicz M, Nogajewski K, Molas M R, Potemski M, Wysmołek A and Babiński A 2016 Raman scattering of few-layers MoTe₂ *2D Mater.* **3** 25010
- [30] Tan Q-H, Zhang X, Luo X-D, Zhang J and Tan P-H 2017 Layer-number dependent high-frequency vibration modes in few-layer transition metal dichalcogenides induced by interlayer couplings *J. Semicond.* **38** 31006
- [31] Fang H, Battaglia C, Carraro C, Nemsak S, Ozdol B, Kang J S, Bechtel H A, Desai S B, Kronast F, Unal A A, Conti G, Conlon C, Palsson G K, Martin M C, Minor A M, Fadley C S, Yablonovitch E, Maboudian R and Javey A 2014 Strong interlayer coupling in van der Waals heterostructures built from single-layer chalcogenides *Proc. Natl. Acad. Sci.* **111** 6198–202
- [32] Rivera P, Schaibley J R, Jones A M, Ross J S, Wu S, Aivazian G, Klement P, Seyler K, Clark G, Ghimire N J, Yan J, Mandrus D G, Yao W and Xu X 2015 Observation of long-lived interlayer excitons in monolayer MoSe₂–WSe₂ heterostructures *Nat. Commun.* **6** 6242
- [33] Duan X, Wang C, Shaw J C, Cheng R, Chen Y, Li H, Wu X, Tang Y, Zhang Q, Pan A, Jiang J, Yu R, Huang Y and Duan X 2014 Lateral epitaxial growth of two-dimensional layered semiconductor heterojunctions *Nat. Nanotechnol.* **9** 1024–30
- [34] Wilson J A and Yoffe A D 1969 The transition metal dichalcogenides discussion and interpretation of the observed optical, electrical and structural properties *Adv. Phys.* **18** 193–335

- [35] Ribeiro-Soares J, Almeida R M, Barros E B, Araujo P T, Dresselhaus M S, Cançado L G and Jorio A 2014 Group theory analysis of phonons in two-dimensional transition metal dichalcogenides *Phys. Rev. B* **90** 115438
- [36] He J, Hummer K and Franchini C 2014 Stacking effects on the electronic and optical properties of bilayer transition metal dichalcogenides MoS₂, MoSe₂, WS₂, and WSe₂ *Phys. Rev. B* **89** 75409
- [37] Zhao W, Ghorannevis Z, Chu L, Toh M, Kloc C, Tan P-H and Eda G 2013 Evolution of Electronic Structure in Atomically Thin Sheets of WS₂ and WSe₂ *ACS Nano* **7** 791–7
- [38] Terrones H, Del Corro E, Feng S, Poumirol J M, Rhodes D, Smirnov D, Pradhan N R, Lin Z, Nguyen M a T, Elías a L, Mallouk T E, Balicas L, Pimenta M a and Terrones M 2014 New first order Raman-active modes in few layered transition metal dichalcogenides. *Sci. Rep.* **4** 4215
- [39] Bromley R A, Murray R B and Yoffe A D 1972 The band structures of some transition metal dichalcogenides. III. Group VIA: trigonal prism materials *J. Phys. C Solid State Phys.* **5** 759
- [40] Beal A R, Knights J C and Liang W Y 1972 Transmission spectra of some transition metal dichalcogenides. II. Group VIA: trigonal prismatic coordination *J. Phys. C Solid State Phys.* **5** 3540–51
- [41] Kozawa D, Kumar R, Carvalho A, Kumar Amara K, Zhao W, Wang S, Toh M, Ribeiro R M, Castro Neto A H, Matsuda K and Eda G 2014 Photocarrier relaxation pathway in two-dimensional semiconducting transition metal dichalcogenides. *Nat. Commun.* **5** 4543

- [42] Li Y, Chernikov A, Zhang X, Rigosi A, Hill H M, van der Zande A M, Chenet D A, Shih E-M, Hone J and Heinz T F 2014 Measurement of the optical dielectric function of monolayer transition-metal dichalcogenides: MoS₂, MoSe₂, WS₂, and WSe₂ *Phys. Rev. B* **90** 205422
- [43] Schmidt R, Niehues I, Schneider R, Drüppel M, Deilmann T, Rohlfing M, de Vasconcellos S M, Castellanos-Gomez A and Bratschitsch R 2016 Reversible uniaxial strain tuning in atomically thin WSe₂ *2D Mater.* **3** 21011
- [44] Frisenda R, Niu Y, Gant P, Molina-Mendoza A J, Schmidt R, Bratschitsch R, Liu J, Fu L, Dumcenco D, Kis A, De Lara D P and Castellanos-Gomez A 2017 Micro-reflectance and transmittance spectroscopy : a versatile and powerful tool to characterize 2D materials *J. Phys. D: Appl. Phys.* **50** 074002
- [45] Zhao Y, Luo X, Li H, Zhang J, Araujo P T, Gan C K, Wu J, Zhang H, Quek S Y, Dresselhaus M S and Xiong Q 2013 Interlayer Breathing and Shear Modes in Few-Trilayer MoS₂ and WSe₂ *Nano Lett.* **13** 1007–15
- [46] Yoon D, Moon H, Son Y-W, Choi J S, Park B H, Cha Y H, Kim Y D and Cheong H 2009 Interference effect on Raman spectrum of graphene on SiO₂/Si *Phys. Rev. B* **80** 125422
- [47] Renucci J B, Tyte R N and Cardona M 1975 Resonant Raman scattering in silicon *Phys. Rev. B* **11** 3885–95
- [48] Beal a R, Liang W Y and Hughes H P 1976 Kramers-Kronig analysis of the reflectivity spectra of 3R-WS₂ and 2H-WSe₂ *J. Phys. C* **89** 2449

- [49] Zhang X, Han W P, Wu J B, Milana S, Lu Y, Li Q Q, Ferrari A C and Tan P H 2013 Raman spectroscopy of shear and layer breathing modes in multilayer MoS₂ *Phys. Rev. B* **87** 115413
- [50] Zhao W, Ghorannevis Z, Amara K K, Pang J R, Toh M, Zhang X, Kloc C, Tan P H and Eda G 2013 Lattice dynamics in mono- and few-layer sheets of WS₂ and WSe₂ *Nanoscale* **5** 9677
- [51] Chen S Y, Zheng C, Fuhrer M S and Yan J 2015 Helicity-Resolved Raman Scattering of MoS₂, MoSe₂, WS₂, and WSe₂ Atomic Layers *Nano Lett.* **15** 2526–32
- [52] Lee C, Yan H, Brus L E, Heinz T F, Hone J and Ryu S 2010 Anomalous lattice vibrations of single- and few-layer MoS₂ *ACS Nano* **4** 2695–700
- [53] Davydov A S 1964 The Theory of Molecular Excitons *Sov. Phys. Uspekhi* **7** 145–78
- [54] Wermuth C G, Ganellin C R, Lindberg P and Mitscher L A 1979 Glossary of Terms Used in Physical Organic Chemistry *Pure Appl. Chem.* **51** 1129–43
- [55] Sekine T, Uchinokura K, Nakashizu T, Matsuura E and Yoshizaki R 1984 Dispersive Raman Mode of Layered Compound 2H-MoS₂ under the Resonant Condition *J. Phys. Soc. Japan* **53** 811–8
- [56] Fano U 1961 Effects of Configuration Interaction on Intensities and Phase Shifts *Phys. Rev.* **124** 1866–78
- [57] Tan P H, Han W P, Zhao W J, Wu Z H, Chang K, Wang H, Wang Y F, Bonini N, Marzari N, Pugno N, Savini G, Lombardo A and Ferrari A C 2012 The shear mode of multilayer graphene *Nat. Mater.* **11** 294–300

- [58] Huang W, Luo X, Gan C K, Quek S Y and Liang G 2014 Theoretical study of thermoelectric properties of few-layer MoS₂ and WSe₂ *Phys. Chem. Chem. Phys.* **16** 10866
- [59] Zeng H, Zhu B, Liu K, Fan J, Cui X and Zhang Q M 2012 Low-frequency Raman modes and electronic excitations in atomically thin MoS₂ films *Phys. Rev. B - Condens. Matter Mater. Phys.* **86** 1–5
- [60] Luo X, Zhao Y, Zhang J, Xiong Q and Quek S Y 2013 Anomalous frequency trends in MoS₂ thin films attributed to surface effects *Phys. Rev. B* **88** 75320

Supplementary Information

Excitonic Resonance Effects and Davydov Splitting in Raman Spectra of Few-Layer WSe₂

Sanghun Kim,[†] Kim Kangwon,[†] Jae-Ung Lee,[†] and Hyeonsik Cheong[†]

[†]Department of Physics, Sogang University, Seoul 04107, Korea

Contents:

- **Figure S1.** Optical microscope images of few-layer WSe₂ samples and photoluminescence (PL) spectra of few-layer WSe₂.
- **Figure S2.** Raman spectra of 1–3TL WSe₂ measured with 8 excitation energies.
- **Figure S3.** Raman spectra of 4–5TL, and 7TL WSe₂ measured with 8 excitation energies.
- **Figure S4.** Raman spectra of 8TL and 12 nm WSe₂ measured with 8 excitation energies.
- **Figure S5.** Thickness dependence of Raman spectrum of WSe₂ measured with excitation energies 1.58 eV, 1.96 eV, and 2.33 eV.
- **Figure S6.** Thickness dependence of Raman spectrum of WSe₂ measured with excitation energies 2.41 eV, 2.54 eV, and 2.71 eV.
- **Figure S7.** Thickness dependence of Raman spectrum of WSe₂ measured with excitation energies 2.81 eV and 3.82 eV.
- **Figure S8.** Raman intensity as a function of excitation energies for the E_{1g}, A_{2u}, 2LA(M), shear, and breathing modes.
- **Figure S9.** Anti-Stokes and Stokes Raman spectra of few-layer WSe₂ measured with 1.58 eV excitation energy.

- **Figure S10.** Breit-Wigner-Fano (BWF) line fitting of Raman spectra near 301 cm^{-1} measured with excitation energy of 1.58 eV.
- **Figure S11.** Photoluminescence (PL) spectra of 1-4 TL WSe₂ with deconvolution of A exciton, trion, and indirect gap transition signals.
- **Figure S12.** Excitation energy dependent low-frequency Raman spectra of 1–5TL and 7TL WSe₂.
- **Figure S13.** Excitation energy dependent low-frequency Raman spectra of 8TL and 12 nm WSe₂.
- **Figure S14.** Raman spectra of the A_{2u} mode measured with excitation energy of 2.81 eV (441.6 nm).

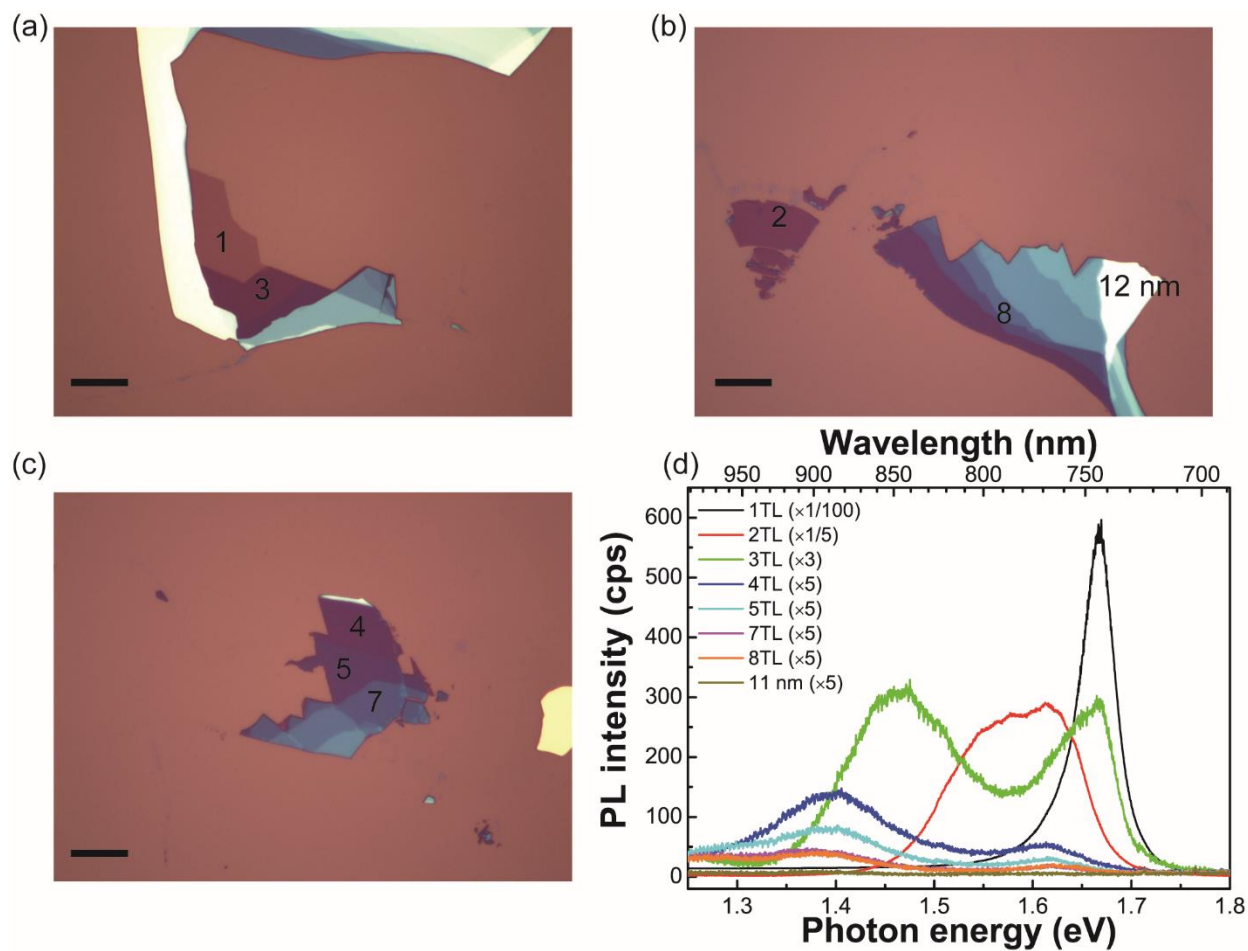


Figure S1. (a), (b), (c) Optical microscope images of few-layer WSe₂ samples. The scale bar is 10 μm and the number of layers of WSe₂ is indicated. (d) Photoluminescence (PL) spectra of few-layer WSe₂.

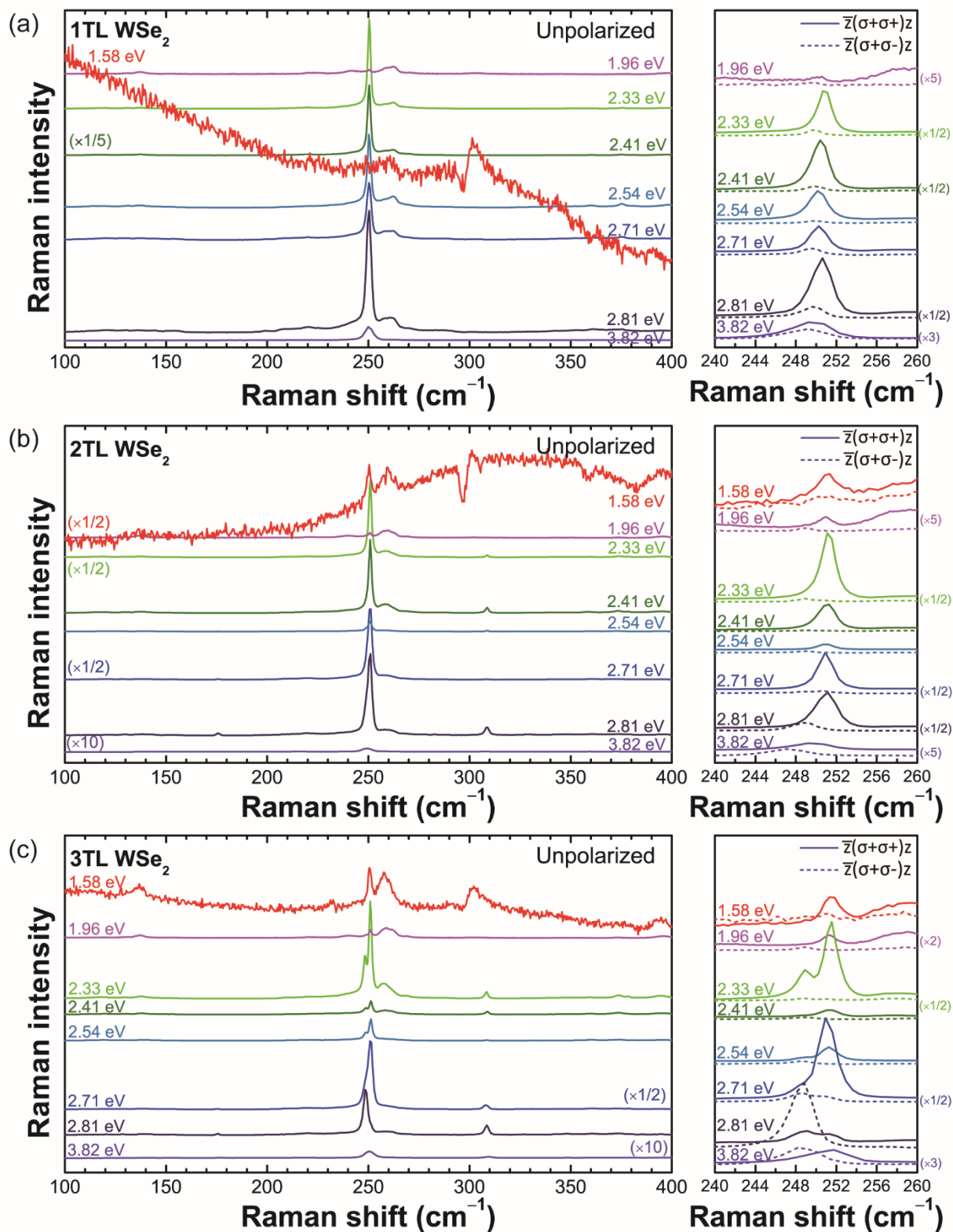


Figure S2. Raman spectra of (a) 1TL, (b) 2TL, and (c) 3TL WSe₂ measured with 8 excitation energies indicated. Circularly polarized Raman results are shown on the right.

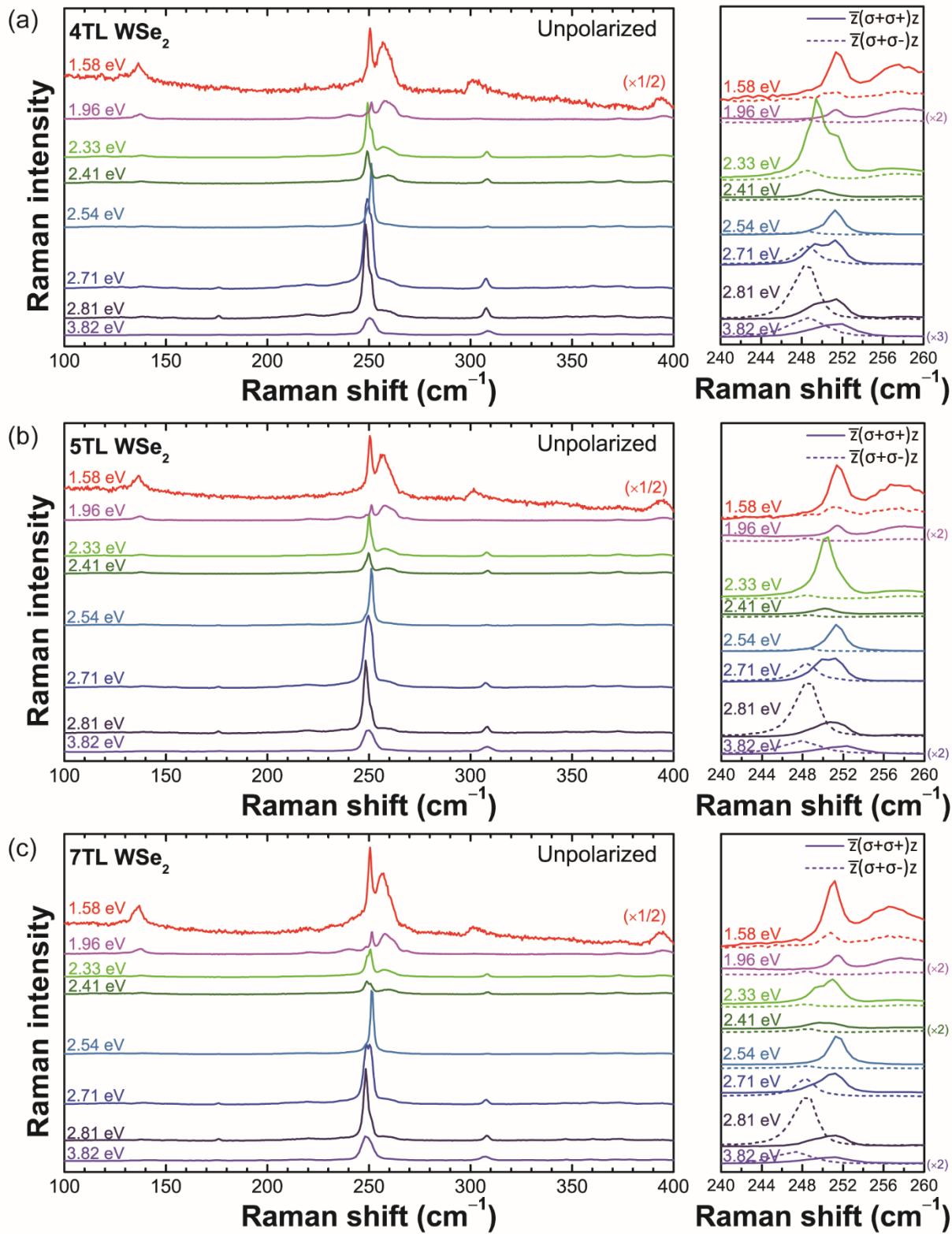


Figure S3. Raman spectra of (a) 4TL, (b) 5TL, and (c) 7TL WSe₂ measured with 8 excitation energies indicated. Circularly polarized Raman results are shown on the right.

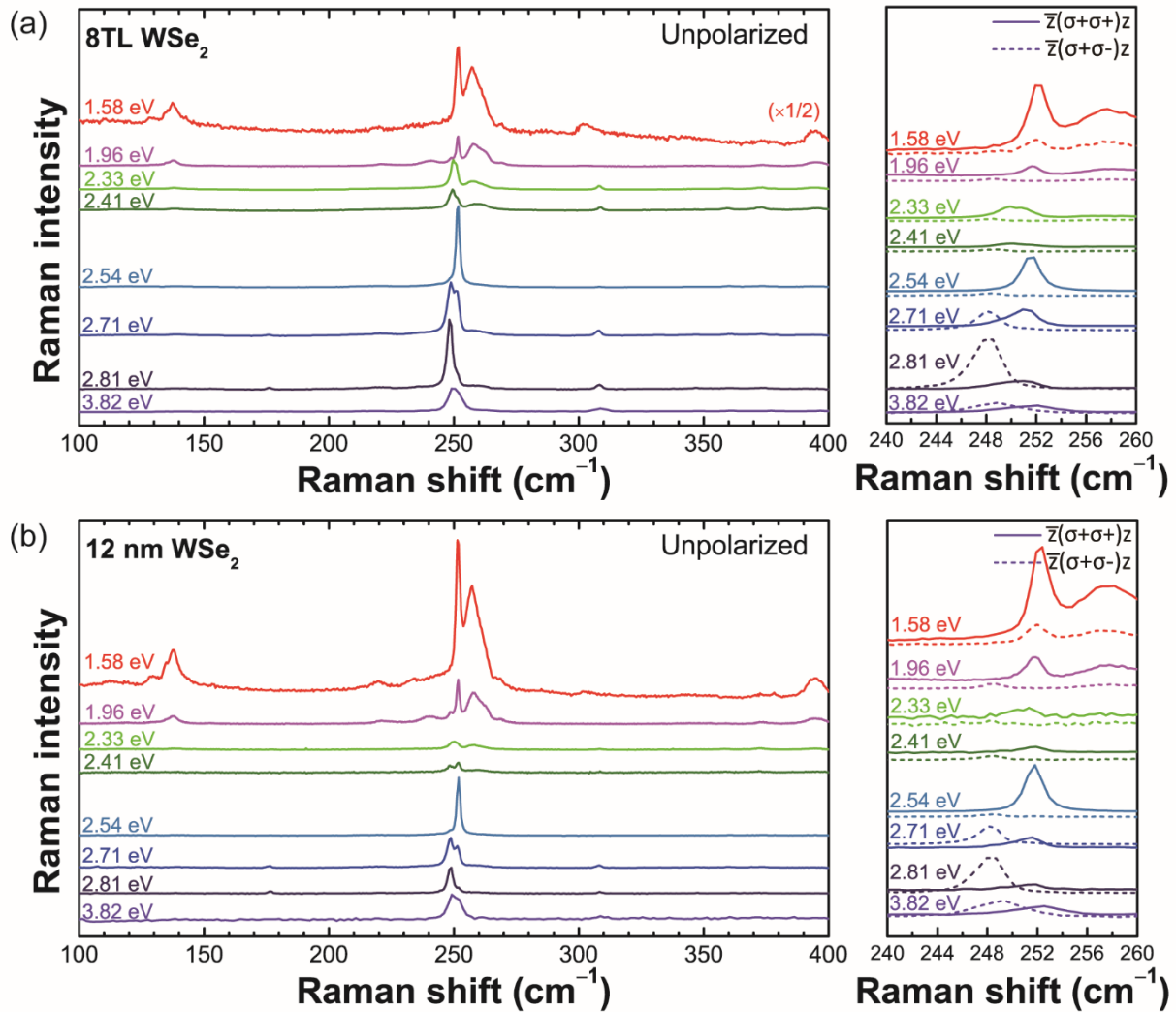


Figure S4. Raman spectra of (a) 8TL and (b) 12 nm WSe₂ measured with 8 excitation energies indicated. Circularly polarized Raman results are shown on the right.

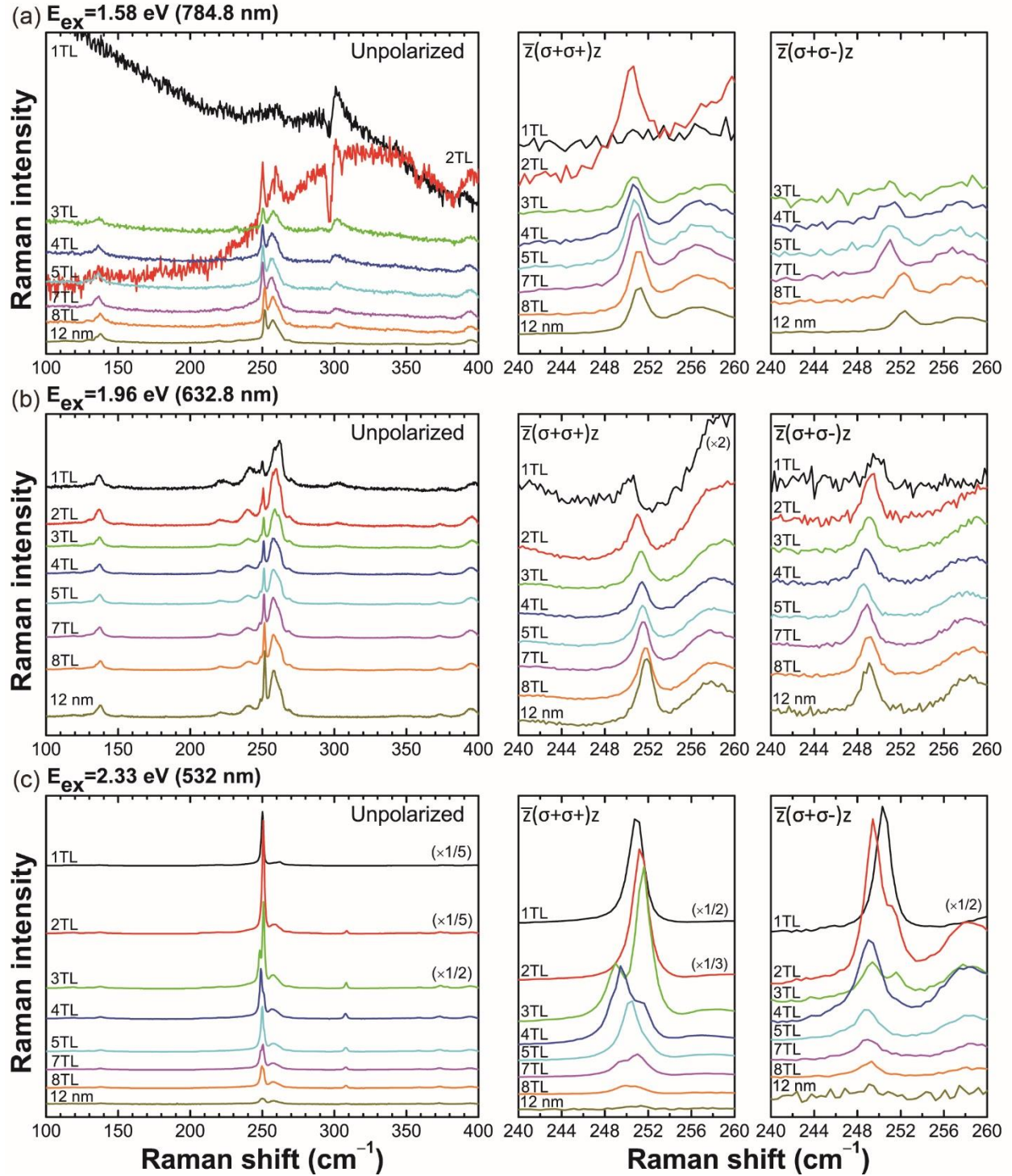


Figure S5. Thickness dependence of the Raman spectrum of WSe₂ measured with excitation energies (a) 1.58 eV, (b) 1.96 eV, and (c) 2.33 eV. Circularly polarized Raman results are shown on the right.

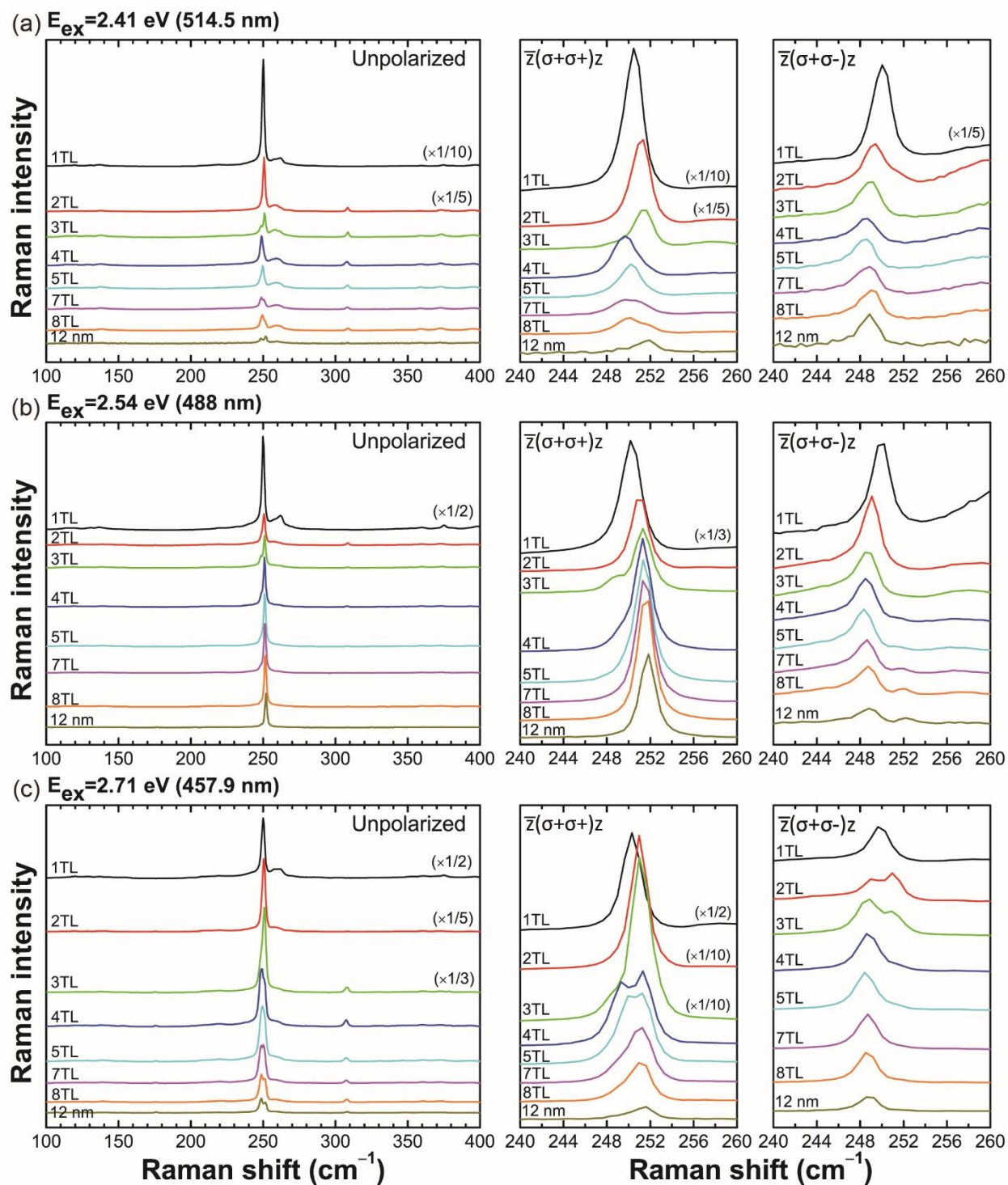


Figure S6. Thickness dependence of the Raman spectrum of WSe₂ measured with excitation energies (a) 2.41 eV, (b) 2.54 eV, and (c) 2.71 eV. Circularly polarized Raman results are shown on the right.

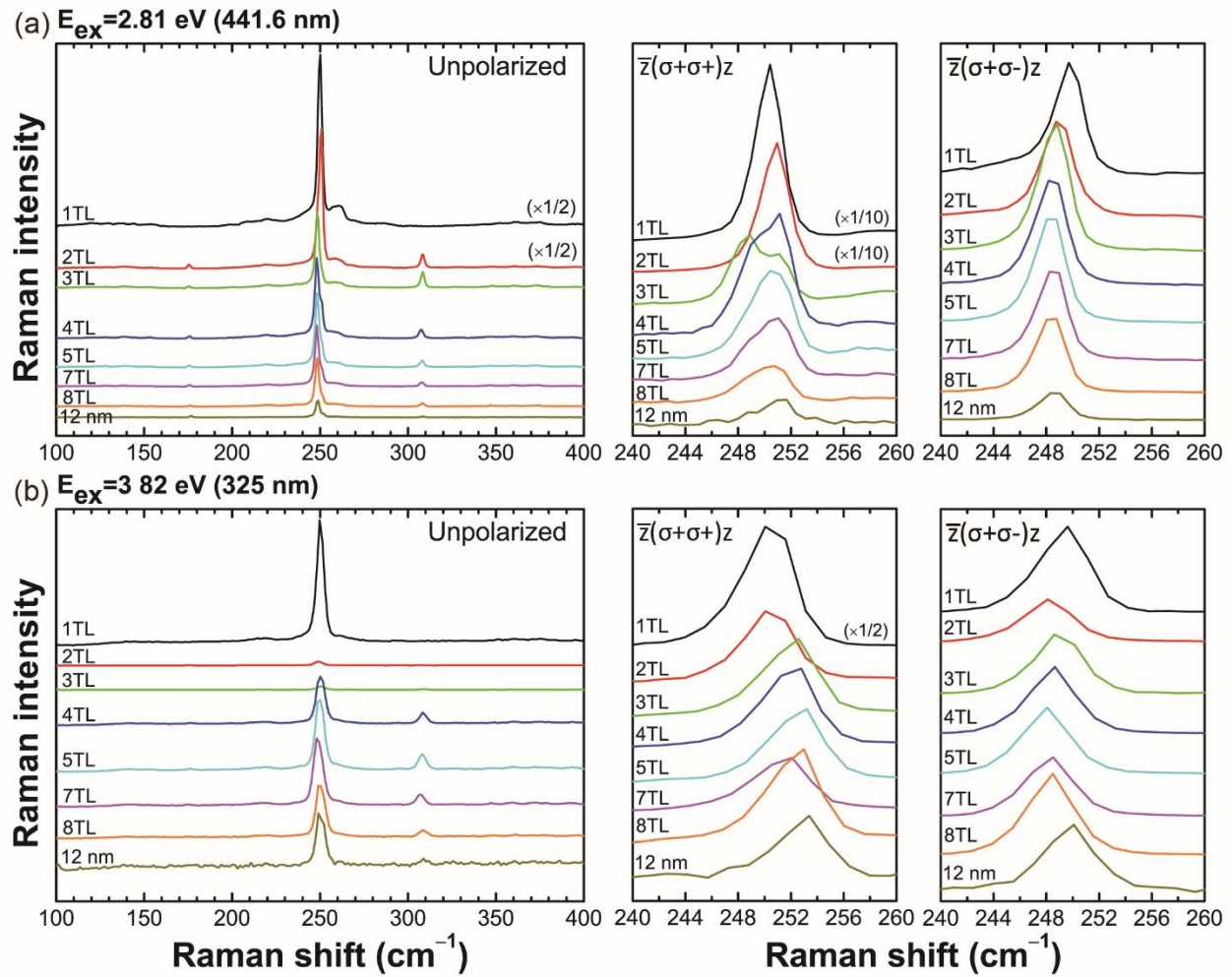


Figure S7. Thickness dependence of the Raman spectrum of WSe₂ measured with excitation energies (a) 2.81 eV and (b) 3.82 eV. Circularly polarized Raman results are shown on the right.

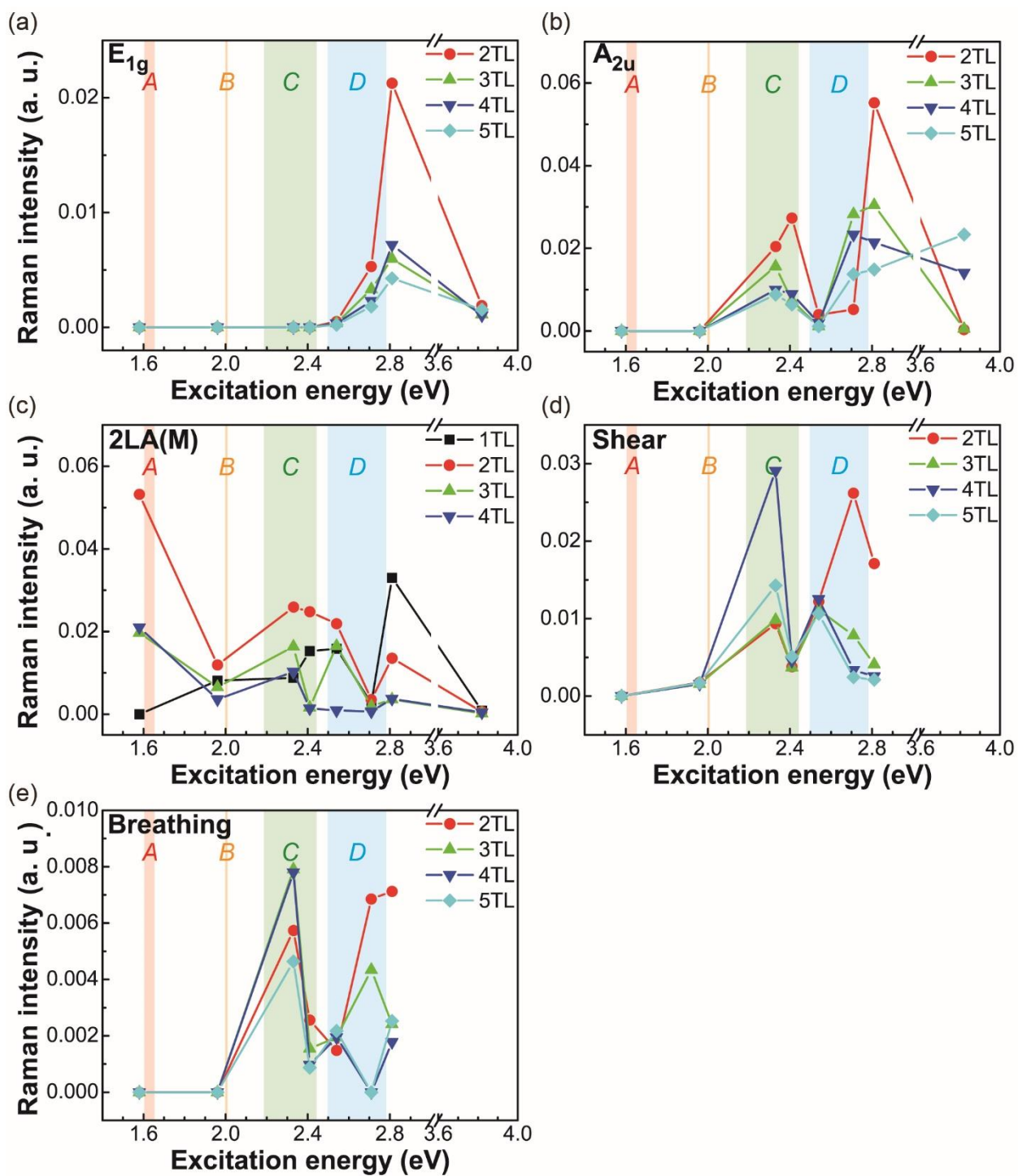


Figure S8. Raman intensity as a function of excitation energies for (a) the E_{1g} , (b) A_{2u} , (c) $2LA(M)$, (d) shear, and (e) breathing modes.

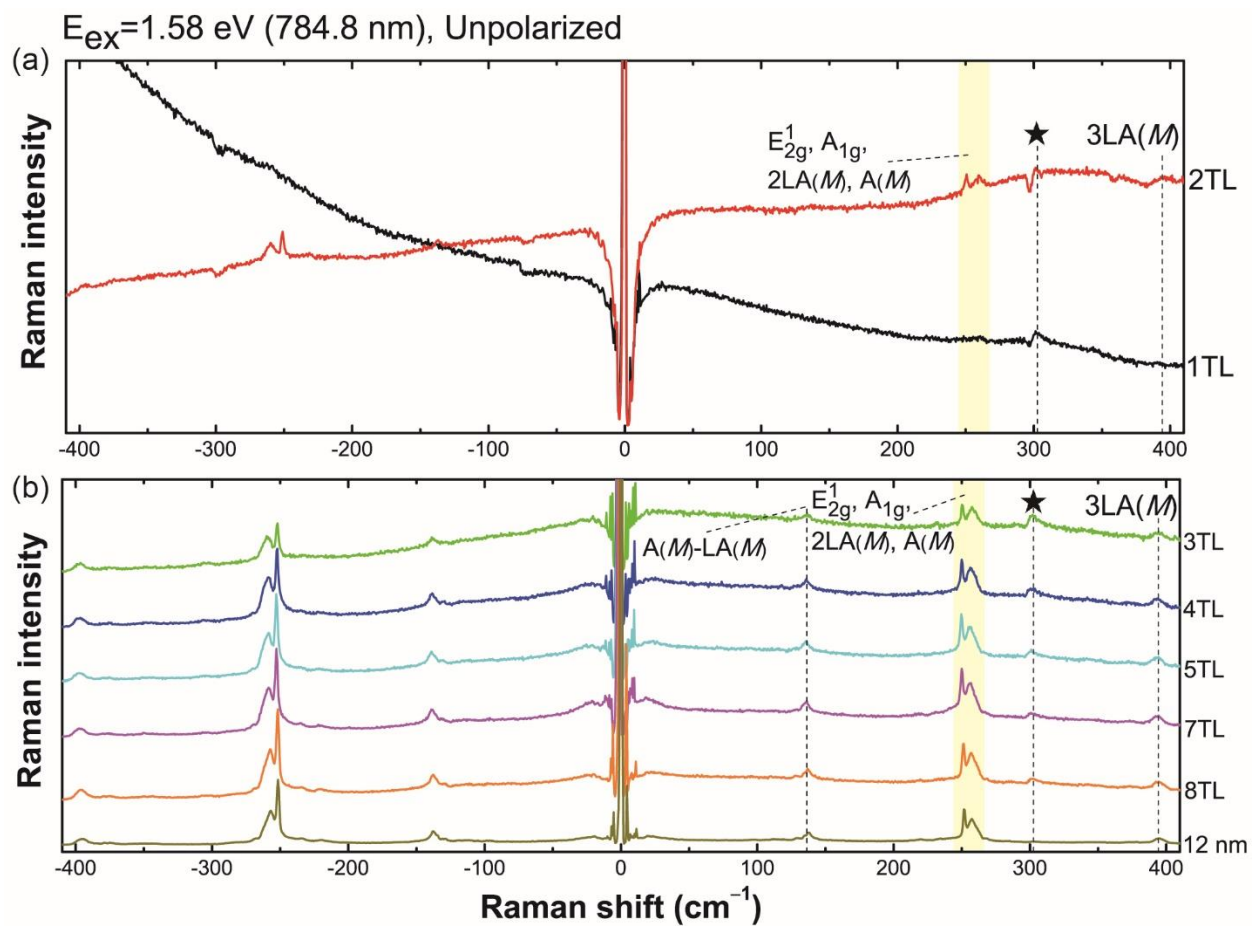


Figure S9. Anti-Stokes and Stokes Raman spectra of few-layer WSe₂ measured with 1.58 eV excitation energy.

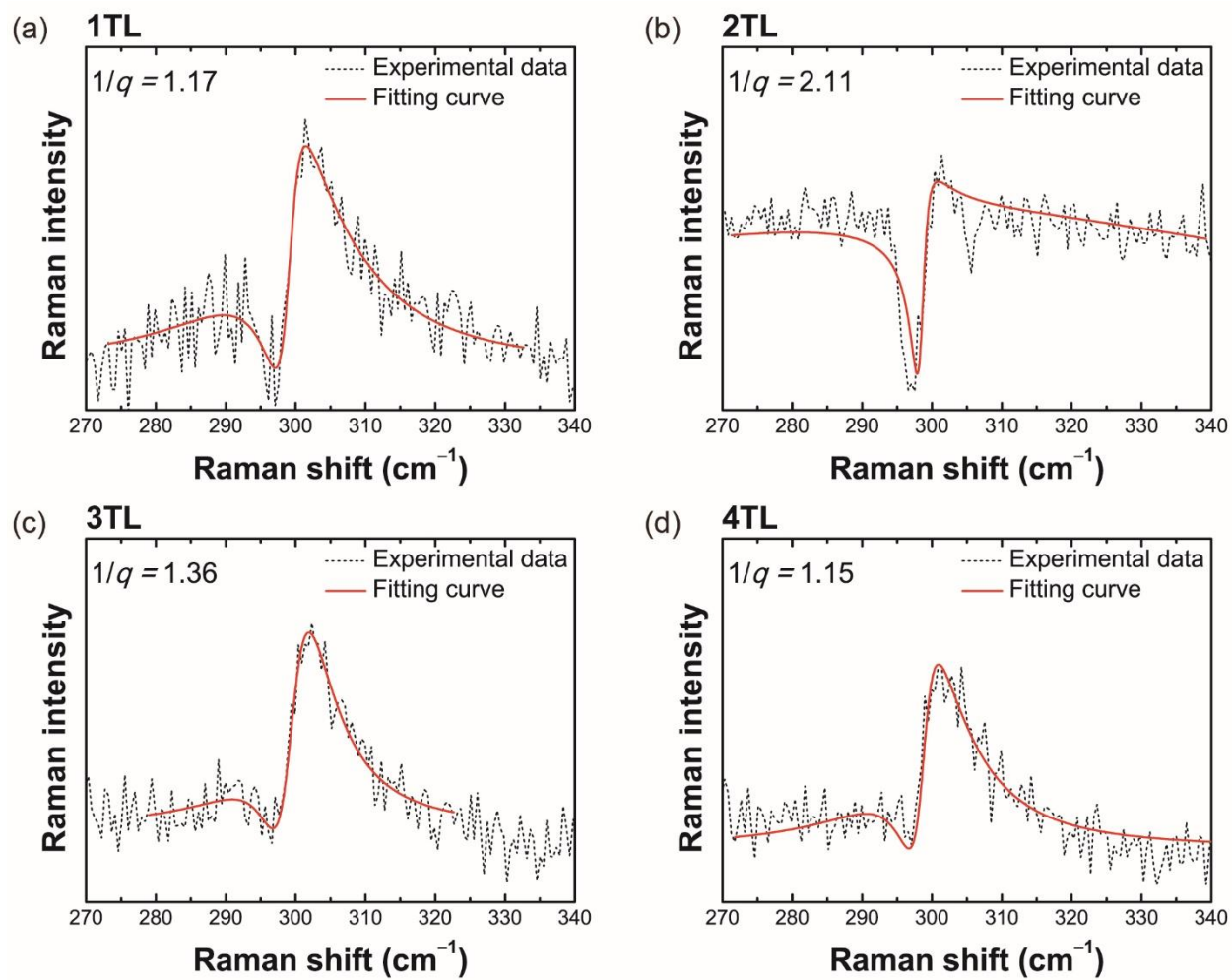


Figure S10. Breit-Wigner-Fano (BWF) line fitting of Raman spectra near 301 cm^{-1} measured with excitation energy of 1.58 eV .

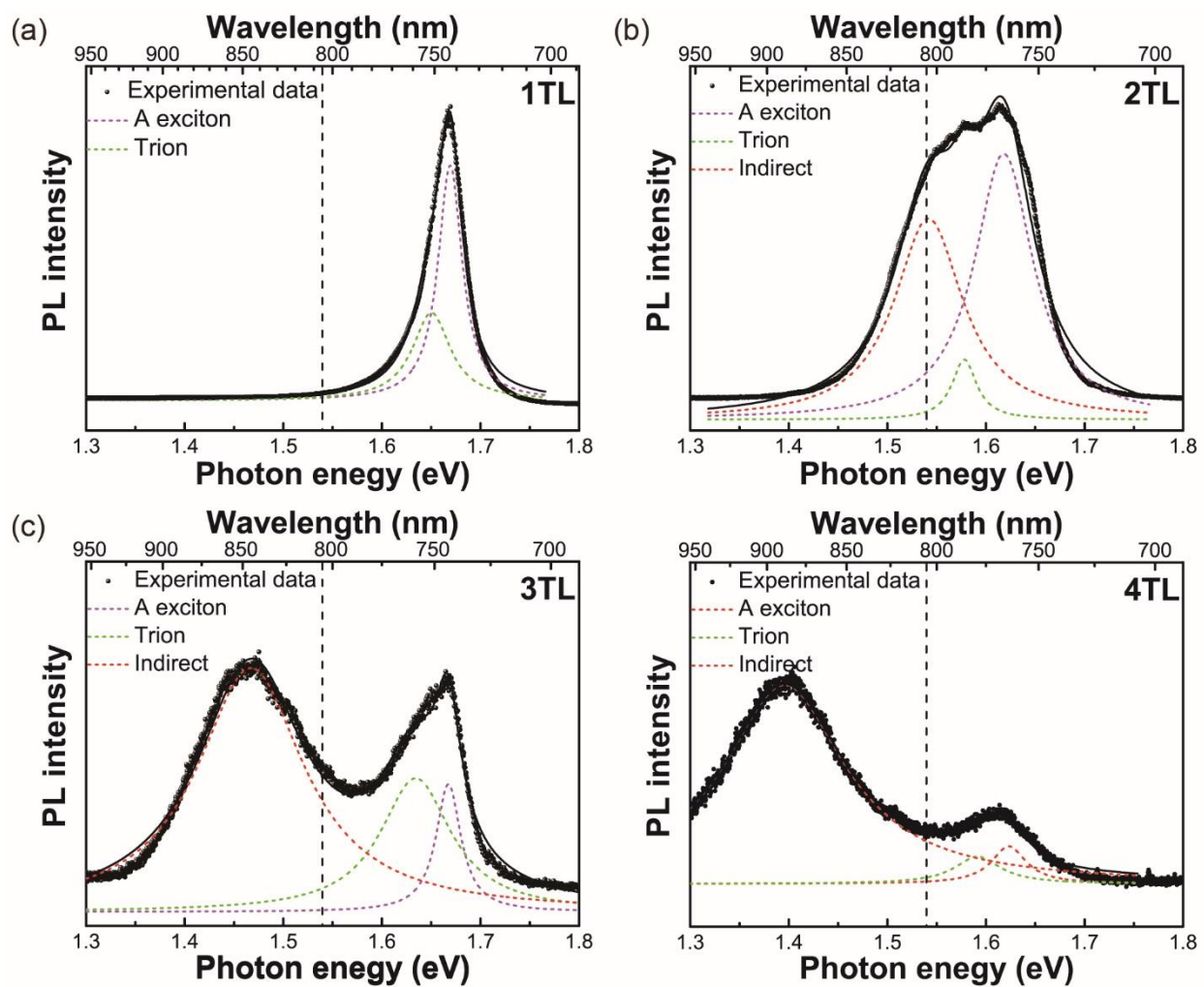


Figure S11. Photoluminescence (PL) spectra of 1-4 TL WSe₂ with deconvolution of A exciton, trion, and indirect gap transition signals. Black dashed line at 1.54 eV indicates the Raman scattered photon energy of the BWF line at 301 cm⁻¹.

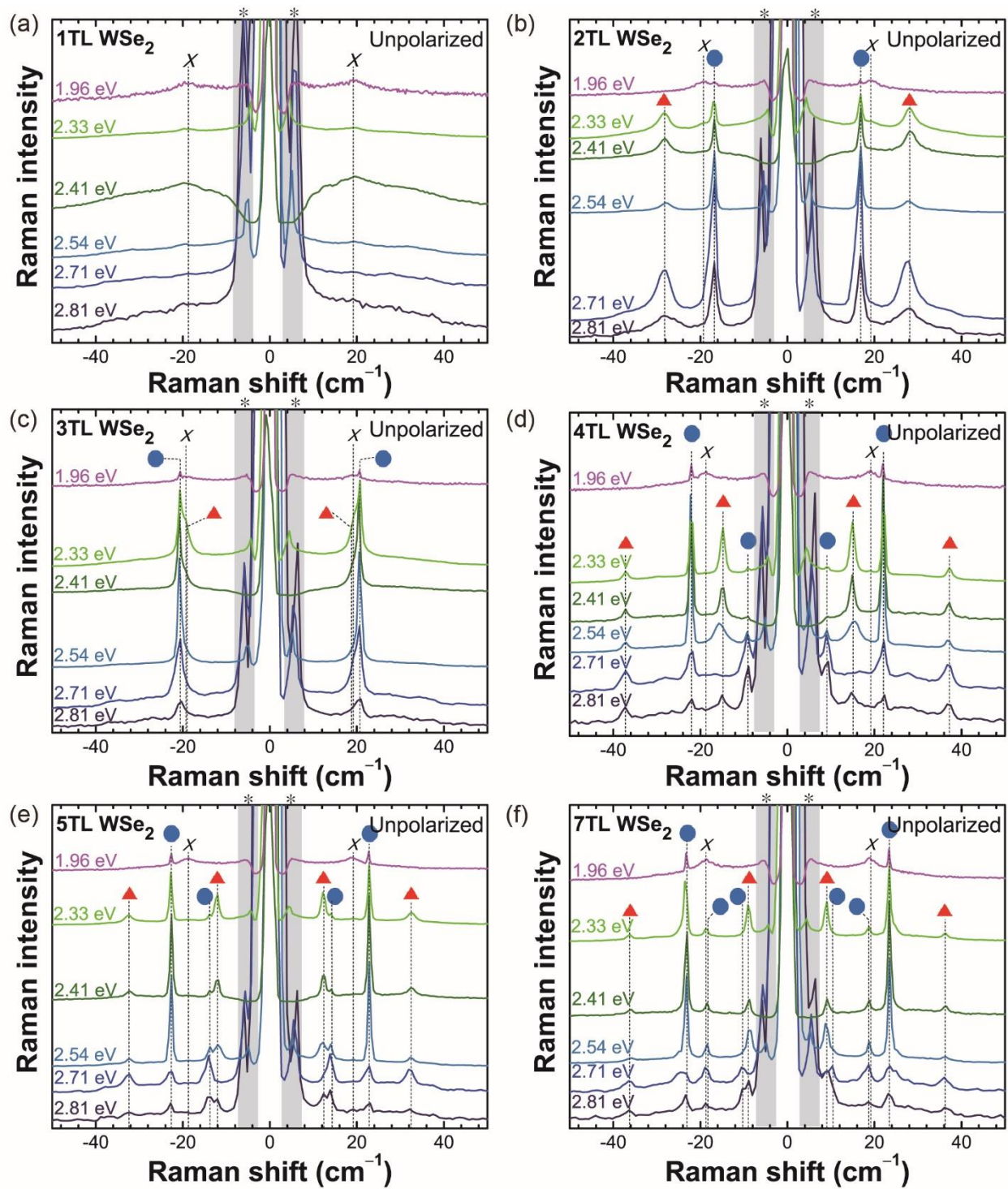


Figure S12. Excitation energy dependent low-frequency Raman spectra of 1–5TL and 7TL WSe₂. The Brillouin scattering peak of the Si substrate is indicated by (*) and the breathing and shear modes are indicated by red triangles and blue circles, respectively.

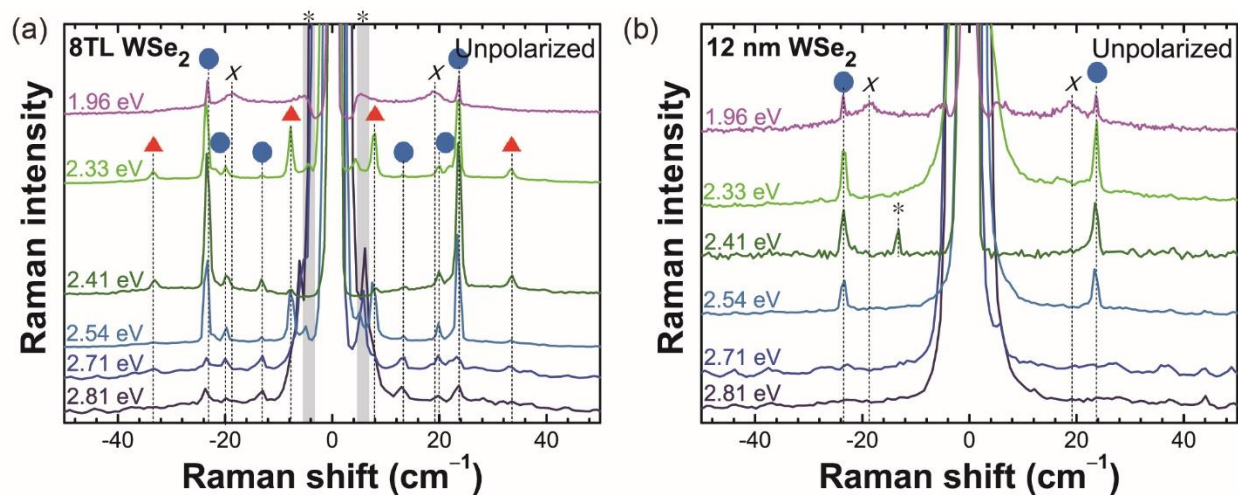


Figure S13. Excitation energy dependent low-frequency Raman spectra of (a) 8TL and (b) 12 nm WSe₂. A plasma line of the 2.41 eV laser is indicated by (*) and the breathing and shear modes are indicated by red triangles and blue circles, respectively.

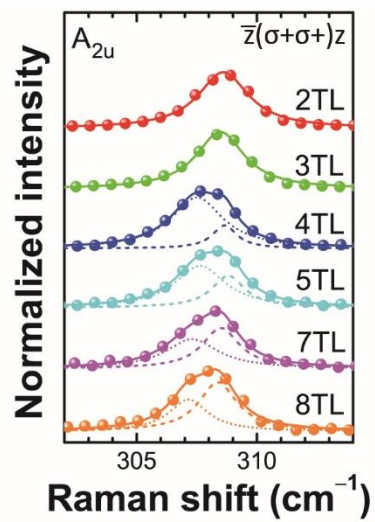


Figure S14. Raman spectra of the A_{2u} mode measured with excitation energy of 2.81 eV (441.6 nm).